

Nonlinear clustering in models with primordial non-Gaussianity: The halo model approachRobert E. Smith,^{1,2,*} Vincent Desjacques,¹ and Laura Marian²¹*Institute for Theoretical Physics, University of Zurich, Zurich CH 8037, Switzerland*²*Argelander-Institute for Astronomy, Auf dem Hügel 71, D-53121 Bonn, Germany*

(Received 27 September 2010; published 24 February 2011; publisher error corrected 3 March 2011)

We develop the halo model of large-scale structure as an accurate tool for probing primordial non-Gaussianity. In this study we focus on understanding the matter clustering at several redshifts in the context of primordial non-Gaussianity that is a quadratic correction to the local Gaussian potential, characterized by the parameter f_{NL} . In our formulation of the halo model we pay special attention to the effect of halo exclusion and show that this can potentially solve the long-standing problem of excess power on large scales in this model. The halo model depends on the mass function, clustering of halo centers, and the density profiles. We test these ingredients using a large ensemble of high-resolution Gaussian and non-Gaussian numerical simulations, covering $f_{\text{NL}} = \{0, +100, -100\}$. In particular, we provide a first exploration of how halo density profiles change in the presence of primordial non-Gaussianity. We find that for f_{NL} positive (negative) high-mass haloes have an increased (decreased) core density, so being more (less) concentrated than in the Gaussian case. We also examine the halo bias and show that, if the halo model is correct, then there is a small asymmetry in the scale dependence of the bias on very large scales, which arises because the Gaussian bias must be renormalized. We show that the matter power spectrum is modified by $\sim 2.5\%$ and $\sim 3.5\%$ on scales $k \sim 1.0 h \text{ Mpc}^{-1}$ at $z = 0$ and $z = 1$, respectively. Our halo model calculation reproduces the absolute amplitude to within $\lesssim 10\%$ and the ratio of non-Gaussian to Gaussian spectra to within $\lesssim 1\%$. We also measure the matter correlation function and find similarly good levels of agreement between the halo model and the data. We anticipate that this modeling will be useful for constraining f_{NL} from measurements of the shear correlation function in future weak lensing surveys such as Euclid.

DOI: 10.1103/PhysRevD.83.043526

PACS numbers: 98.80.-k

I. INTRODUCTION

Over the last few decades, through experiments such as 2dFGRS, SDSS, and WMAP [1–3], great strides have been made in quantifying the parameters of the perturbed and unperturbed Friedmann-Lemaître-Robertson-Walker model. Besides the detailed information about the present Universe, these experiments have also opened up important new windows into the physics of the early Universe.

The inflationary paradigm is so far the leading physical explanation for the origins of structure. The single-field slow-roll theory makes four fundamental predictions: a flat universe (quantified by the curvature density parameter Ω_K); a primordial density power spectrum with power-law index (n_s) just less than unity; a nearly Gaussian distribution of primordial density fluctuations (deviation from Gaussianity being quantified by the f_{NL} parameter); a spectrum of gravitational waves (characterized by the amplitude of the quadrupole tensor to scalar ratio r). The measurement of the CMB temperature anisotropies combined with a number of cosmological probes, such as the baryonic acoustic oscillation (BAO) scale in the SDSS luminous red galaxies, and the present-day value of the Hubble constant, provide strong supporting evidence in favor of the first three of these predictions. The current

WMAP7 + BAO + H_0 combined constraints on these parameters are [4] $-0.0133 < \Omega_K < 0.0084$ (95% C.L.), $n_s = 0.963 \pm 0.012$ (68% C.L.), and $f_{\text{NL}} = 32 \pm 21$ (68% C.L.). For the spectrum of gravitational waves current CMB experiments (WMAP7 + ACBAR + QUaD) place an upper bound of $r < 0.33$ (95% C.L.) [4–6]. The latter can only be further falsified with dedicated CMB polarization experiments such as Planck [7].

Intriguingly, the constraints on the amount of primordial non-Gaussianity (hereafter, PNG) from the CMB are tightening around a nonzero value, there currently being $\sim 1.5\sigma$ evidence against pure Gaussian scalar perturbations [4] (see also [8] which claimed a 99.5% C.L. detection of nonzero f_{NL}). If f_{NL} is found to be substantially greater than zero at high significance, then this would rule out *all* inflation models based on a single scalar field [9]. On the other hand, multifield models may produce large levels of PNG and also scale-dependent f_{NL} . Thus testing the Gaussianity of the initial fluctuations is of prime concern.

Most tests for PNG have primarily been performed on the temperature anisotropies in the CMB; however, for several decades it has been theoretically understood that PNG also affects a number of large-scale structure observables [10–13]. However, very few tests with real galaxy survey data have been performed. This was primarily due to the fact that in the present-day Universe the density fluctuations do not remain pristine but have been driven

*res@physik.unizh.ch

to a non-Gaussian state by gravity. Gravitational evolution of the density perturbations correlates the amplitudes and phases of different Fourier modes, and thus one is faced with the problem of decoupling primordial from gravitational non-Gaussianity. Furthermore, in observing large-scale structures one does not in general get information about all points in space, but instead one is restricted to learning only about the galaxy distribution. In general this is related to the underlying density statistics through a bias function (or functional), which may be complicated and stochastic. In the simple case of deterministic local biasing, one may attempt to use higher order statistics such as the galaxy bispectrum to disentangle the effects of gravity and galaxy bias [14–17]. However, no constraints on f_{NL} have yet emerged from such schemes. This partly owes to the fact that past survey volumes have been too small for such tests to be performed with any confidence. The survey volumes of ongoing and future planned missions will surely change this.

Recently, in a ground-breaking paper, it was shown both theoretically and in numerical simulations by [18] that there is a strong signature of f_{NL} in the power spectrum of dark matter haloes. The effect is to induce a scale-dependent bias correction $\Delta b \propto k^{-2}$. The exciting prospect of this is that, since the signature affects primarily only the largest scales $k < 0.02 h \text{ Mpc}^{-1}$, one can in principle decouple the effects induced by nonlinear bias and gravity from those of PNG and so constrain the latter. There has been much activity in quantifying the effects of this scale-dependent bias on the power spectrum in simulations [19–21]; and also there has been much theoretical activity to truly understand how the scale-dependent bias arises [22–26], and for a current review see [27]. This has culminated in several recent attempts to constrain f_{NL} from large-scale structure data [22,28,29].

Another recent result has shown that the nonlinear dark matter power spectrum alone is sensitive to the presence of f_{NL} [16,17,19,21,30]. This prompted [31] to propose that the statistics of the initial conditions could be tested through weak gravitational lensing by large-scale structure, in particular, through measurement of the two-point shear correlation functions. The advantage of such a probe is that it is only sensitive to the total mass distribution projected along the line of sight. On the down side, the signal is weak, with deviations being of the order of several percent. However, future all sky weak lensing surveys such as EUCLID [32] and LSST [33] will be able to probe changes in the convergence power spectrum to percent level accuracy. It is therefore of great interest to quantify in detail how sensitive such a mission would be to constraining PNG of the local type. The starting point for such a study is an accurate model of the matter power spectrum as a function of redshift.

In this study we focus on understanding how PNG shapes the two-point matter clustering statistics in

Fourier and configuration space. Currently there is no accurate analytic model for describing the effects of PNG on the matter power spectrum over the range of scales that will be required for future weak lensing missions ($k \in [0.01, 100.0] h \text{ Mpc}^{-1}$ [34,35]). This we shall attempt to build. Following [31], [36] proposed that the halo model might be able to predict the power spectrum. They suggested that PNG would modify predictions in two ways: through the abundance of massive clusters and through the scale-dependent bias. No attempt to compare their model with numerical simulations was presented and so it remains an open question as to how reliable this proposition is. Moreover, they assumed that halo profiles are not affected by PNG. In this work we show, through detailed numerical simulations, that this assumption is wrong and that there are important effects which need to be taken into account if the halo model is to be used to make accurate predictions.

Furthermore, we make important new developments in the importance of halo exclusion in order to make robust predictions, and we show for the first time how this may also resolve a long-standing problem with the halo model, the excess power on large scales.

Last, when exploring how the scale-dependent bias from PNG enters the halo model framework, we have shown that if the model is to be self-consistent, then there must be a modification to the original formula of [18]. This modification creates an asymmetry in the bias for models with the same value of f_{NL} but with an opposite sign. This arises due to the fact that it is not the Gaussian bias which enters the formula of Dalal *et al.* but in fact the total non-Gaussian scale-independent bias. We believe that inclusion of this effect will slightly modify current constraints on f_{NL} .

The paper is broken down as follows: In Sec. II we overview the local model for PNG and its impact on density statistics. In Sec. III we describe the suite of N -body simulations used in this study. In Sec. IV we explore the perturbation theory approach to modeling the matter power spectrum before moving on to describe the halo model. In Sec. V we perform a phenomenological study of the necessary ingredients of the halo model and their dependence on PNG. In Sec. VI we present our predictions for the halo model power spectrum as a function of redshift and also the two-point correlation function. Finally, in Sec. VII we summarize our findings and conclude.

II. PRIMORDIAL NON-GAUSSIANITY

A. Potential statistics

We shall be working with the local model of PNG; that is, we consider only local quadratic corrections to the gauge invariant Bardeen’s potential perturbation, which on scales smaller than the horizon size reduces to minus the Newtonian potential [13]:

$$\Phi(\mathbf{x}) = \phi(\mathbf{x}) + f_{\text{NL}}[\phi(\mathbf{x})^2 - \langle \phi^2(\mathbf{x}) \rangle], \quad (1)$$

where $\phi(x)$ is the Gaussian potential perturbation after matter radiation equality, scaled in terms of units of c^2 to yield a dimensionless quantity. Following standard convention, it is defined to be related to the Newtonian potential as $\Phi(\mathbf{x}) \equiv -\Phi_{\text{Newton}}(\mathbf{x})$. The term $\langle \phi^2(x) \rangle$ is subtracted to ensure that Φ is a mean zero field. In the linear theory the typical fluctuations are of the order of $\Phi \sim 10^{-5}$, and so the non-Gaussian corrections are of the order of $\sim 0.1\%(f_{\text{NL}}/100)(\phi/10^{-5})$.

This transformation of the Gaussian potential leads to a small correction to the power spectrum, but its main effect is to generate a primordial potential bispectrum. To see this consider the Fourier transform of Eq. (1):

$$\Phi(\mathbf{k}) = \phi(\mathbf{k}) + f_{\text{NL}} \int \frac{d^3\mathbf{q}}{(2\pi)^3} \phi(\mathbf{q})\phi(\mathbf{k} - \mathbf{q}). \quad (2)$$

The power spectrum, defined as $\langle \Phi(\mathbf{k}_1)\Phi(\mathbf{k}_2) \rangle \equiv P_\Phi(|\mathbf{k}_1|)(2\pi)^3 \delta^D(\mathbf{k}_1 + \mathbf{k}_2)$ for this field, is given by

$$P_\Phi(\mathbf{k}_1) = P_\phi(\mathbf{k}_1) + 2f_{\text{NL}}^2 \int \frac{d^3\mathbf{q}_1}{(2\pi)^3} P_\phi(\mathbf{q}_1)P_\phi(|\mathbf{k}_1 - \mathbf{q}_1|). \quad (3)$$

The three-point function in Fourier space is given by

$$\begin{aligned} &\langle \Phi(\mathbf{k}_1)\Phi(\mathbf{k}_2)\Phi(\mathbf{k}_3) \rangle \\ &= f_{\text{NL}} \int \frac{d^3\mathbf{q}_3}{(2\pi)^3} \langle \phi(\mathbf{k}_1)\phi(\mathbf{k}_2)\phi(\mathbf{q}_3)\phi(\mathbf{k}_3 - \mathbf{q}_3) \rangle \\ &\quad + 2\text{cyc} + f_{\text{NL}}^3 \int \frac{d^3\mathbf{q}_1}{(2\pi)^3} \frac{d^3\mathbf{q}_2}{(2\pi)^3} \frac{d^3\mathbf{q}_3}{(2\pi)^3} \langle \phi(\mathbf{q}_1)\phi(\mathbf{k}_1 - \mathbf{q}_1) \\ &\quad \times \phi(\mathbf{q}_2)\phi(\mathbf{k}_2 - \mathbf{q}_2)\phi(\mathbf{q}_3)\phi(\mathbf{k}_3 - \mathbf{q}_3) \rangle. \end{aligned} \quad (4)$$

Recall that the expectation value of odd powers of the Gaussian variables vanish, and from Wick's theorem we have that the even powers can be written as $\langle \phi(\mathbf{k}_1) \dots \phi(\mathbf{k}_n) \rangle = \sum_{\text{all pairs}} \prod_{i=1}^{\text{pairs}} \langle \phi(\mathbf{k}_i)\phi(-\mathbf{k}_i) \rangle$. Also, defining the bispectrum as $\langle \Phi(\mathbf{k}_1)\Phi(\mathbf{k}_2)\Phi(\mathbf{k}_3) \rangle \equiv B_\Phi(\mathbf{k}_1, \mathbf{k}_2, \mathbf{k}_3)(2\pi)^3 \delta^D(\mathbf{k}_1 + \mathbf{k}_2 + \mathbf{k}_3)$, then we find the primordial potential bispectrum to be

$$\begin{aligned} B_\Phi(\mathbf{k}_1, \mathbf{k}_2, \mathbf{k}_3) &= 2f_{\text{NL}}[P_\phi(\mathbf{k}_1)P_\phi(\mathbf{k}_2) + 2\text{cyc}] \\ &\quad + 4f_{\text{NL}}^3 \int \frac{d^3\mathbf{q}_1}{(2\pi)^3} P_\phi(\mathbf{q}_1)P_\phi(|\mathbf{q}_1 - \mathbf{k}_1|) \\ &\quad \times [P_\phi(|\mathbf{q}_1 + \mathbf{k}_2|) + P_\phi(|\mathbf{q}_1 + \mathbf{k}_3|)]. \end{aligned} \quad (5)$$

Restricting our attention to the case where $f_{\text{NL}} < 100$, then we may safely neglect the second terms on the right-hand side of Eqs. (3) and (5) [37].

B. Density statistics

The primordial matter potential and density fluctuations, extrapolated to the present day, can be related through Poisson's equation:

$$\begin{aligned} \nabla^2 \Phi(\mathbf{x}, a) &= -\frac{4\pi G}{c^2} [\rho(\mathbf{x}, a) - \bar{\rho}(a)]a^2 \\ &= -\frac{3}{2}\Omega_0 \left(\frac{H_0}{c}\right)^2 \frac{D(a)}{a} \delta_0(\mathbf{x}, a_0), \end{aligned} \quad (6)$$

where a is the expansion factor, $\bar{\rho}(a) = \Omega(a)\rho_{\text{crit}}(a) \propto a^{-3}$ is the mean density of the Universe, $\Omega(a)$ is the density parameter, $\rho_{\text{crit}}(a)$ is the critical density, $H(a)$ is the Hubble parameter, $D(a)$ is the linear growth factor normalized to be unity at the present time, and quantities labeled with a subscript 0 are to be evaluated at the present time a_0 . This equation may be solved in Fourier space to give an explicit relation for the potential:

$$\Phi(\mathbf{k}, a) = \frac{3}{2} \frac{\Omega_0}{k^2} \left(\frac{H_0}{c}\right)^2 \left(\frac{D(a)}{D_0}\right) \left(\frac{a_0}{a}\right) \delta_0(\mathbf{k}, a_0). \quad (7)$$

Evolving the potential back to the initial epoch a_i , and dividing the transfer function, then we have the following relation between the present-day density and primordial potential perturbations:

$$\delta_0(\mathbf{k}, a_0) = \alpha(k, a_i, a_0)\Phi(\mathbf{k}, a_i), \quad (8)$$

where we have defined

$$\alpha(k, a_i, a_0) \equiv \frac{2c^2 g(a_i, a_0) k^2 T(k, a_0)}{3\Omega_0 H_0^2}. \quad (9)$$

In the above equation $g(a_1, a_2) \equiv [D(a_2)/D(a_1)][a_1/a_2]$ is the growth suppression factor ($a_1 < a_2$), and for Λ CDM, $g(a_i, a_0) \approx 0.75$.

In possession of the mapping from the present-day density to primordial potential perturbations through Eq. (8), we may now examine the statistics of the density field. The most important statistic that we will need to know is the present-day skewness filtered on the mass scale M . Following Appendix A, this can be written

$$\begin{aligned} \langle \delta_M^3(x, a_0) \rangle &= 6f_{\text{NL}} \int \frac{dk_1}{2\pi^2} k_1^2 W(k_1, M) \alpha(k_1) P_\phi(k_1) \\ &\quad \times \int \frac{dk_2}{2\pi^2} k_2^2 W(k_2, M) \alpha(k_2) P_\phi(k_2) \frac{1}{2} \\ &\quad \times \int_{-1}^1 d\mu W(k_3, M) \alpha(k_3), \end{aligned} \quad (10)$$

where $k_3^2 \equiv k_1^2 + k_2^2 + 2k_1 k_2 \mu$, $W(k, M)$ is a filter function that selects the mass scale M , and for brevity we shall make the definitions $P_\phi(k_2) \equiv P_\phi(k_2, a_i)$ and $\alpha(k) \equiv \alpha(k, a_i, a_0)$. In what follows we shall also make use of the reduced skewness, defined to be $S_3(M) \equiv \langle \delta_M^3(x) \rangle / \langle \delta_M^2(x) \rangle^2$. Finally, for completeness, we may write the density power spectrum at some arbitrary epoch a in terms of the primordial potential power spectrum simply as

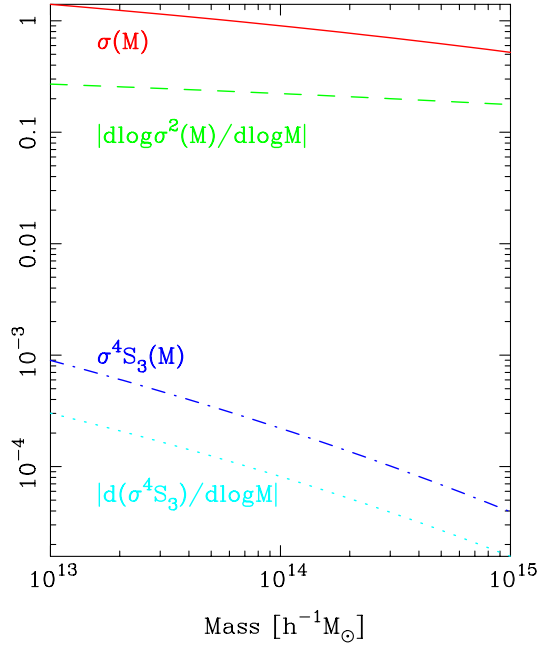


FIG. 1 (color online). Statistical description of the present-day non-Gaussian density field, with $f_{\text{NL}} = 1$, as a function of Lagrangian mass scale M . The solid line shows the standard deviation of the density field; the dot-dashed line shows the skewness of the density field; the dashed and dotted lines show the logarithmic derivatives of these quantities.

$$\begin{aligned} P_\delta(k, a) &= D^2(a, a_0) \alpha^2(k, a_i, a_0) P_\phi(k, a_i) \\ &= D^2(a) \alpha^2(k) P_\phi(k). \end{aligned} \quad (11)$$

In Fig. 1 we show the present-day skewness of the density field $S_3(M) \sigma^4(M)$, as given by Eq. (10) and with $f_{\text{NL}} = 1$. For the calculation we employ a real-space spherical top-hat filter with radius given by the mass scale $R = (3M/4\pi\bar{\rho})^{1/3}$, which in Fourier space has the form $W(y) = (3/y)[\text{siny} - y \text{cosy}]$, where $y \equiv kR$. The figure shows that the skewness is very small, $\lesssim 10^{-3}$ for $R \sim 5 h^{-1} \text{Mpc}$; and if $f_{\text{NL}} = 100$, it is $\lesssim 0.1$.

III. THE N -BODY SIMULATIONS

In order to explore the impact of PNG on the clustering statistics of the density field, we have generated a large ensemble of high-resolution N -body simulations of the Λ CDM cosmology seeded with Gaussian and non-Gaussian initial conditions. This set is an augmented version of the ensemble used by Desjacques, Seljak, and Iliev [19] to study the mass function of cold dark matter (CDM) haloes and their bias and in Sefusatti, Crocce, and Desjacques [17] to explore the matter bispectrum.

The non-Gaussianity in the simulations is of the local form [cf. Eq. (1)], and we use 12 sets of three simulations, each of which has $f_{\text{NL}} = 0, \pm 100$. Each simulation was run with $N = 1024^3$ particles in boxes of side

$L = 1600 h^{-1} \text{Mpc}$ and $V_{\text{Sim}} \sim 4.096 h^{-3} \text{Gpc}^3$, and this gives us a total simulated volume of $V_{\text{Tot}} \sim 49.152 h^{-3} \text{Gpc}^3$. The interparticle forces were softened on scales of 0.04 times the mean interparticle distance, which corresponds to $l_{\text{soft}} \approx 40 h^{-1} \text{kpc}$. We used the WMAP5 cosmological parameters $\{h = 0.7, \Omega_m = 0.279, \Omega_b = 0.0462, n_s = 0.96\}$, and a normalization of the curvature perturbations $\Delta_{\mathcal{R}}^2(k) = 2.21 \times 10^{-9} (k/k_0)^{n_s-1}$, with $k = 0.02 \text{Mpc}^{-1}$, where the curvature perturbation is related to the scalar potential $\mathcal{R} = 5\Phi/3$, and Φ was defined in Eq. (1). In terms of the variance of matter fluctuations linearly extrapolated to the present day, this gives $\sigma_8 \approx 0.81$, where the variance is computed with a spherical top-hat filter of comoving radius $R = 8 h^{-1} \text{Mpc}$.

The matter transfer function was generated using CAMB [38]. All of the simulations were run using the N -body code GADGET-2 [39]. The same Gaussian random seed field ϕ is employed for each $f_{\text{NL}} = \{0, +100, -100\}$ simulation set and varied between sets. This allows the sampling variance between different models of f_{NL} to be minimized when we construct statistics from the ratios of observables. The initial particle distribution was generated at redshift $z_i = 99$ using the Zel'dovich approximation [40].

Regarding the generation of the initial conditions for the non-Gaussian simulations, we adopt the standard (CMB) convention in which $\Phi(\mathbf{x})$ is primordial and not extrapolated to the present epoch. Furthermore, we point out that the local transformation to the potential given by Eq. (1) is performed before multiplication by the matter transfer function $T(k)$.

Dark matter halo catalogs were generated for all snapshots of each simulation using the friends-of-friends (FoF) algorithm [41]. We set the linking-length parameter to the standard $b = 0.2$, where b is the fraction of the interparticle spacing. For this we used the fast parallel B-FOF code, kindly provided by V. Springel. The minimum number of particles for which an object was considered to be a bound halo was set to 20 particles. With particle mass $m_p \approx 3.0 \times 10^{11} h^{-1} M_\odot$, this gave us a minimum host halo mass of $6 \sim 10^{12} M_\odot/h$ [42].

IV. MODELING THE NONLINEAR POWER SPECTRUM

A. Gravitational perturbation theory

The nonlinear evolution of the density field can be followed using the gravitational perturbation theory. In this approach one writes down the equations of motion for the CDM fluid in an expanding spacetime and looks for a series expansion in the density and velocity divergence of the CDM fluid (for a review of the subject see [44]). The important point to note is that the perturbative solutions do not change when we consider the case of structure formation in models with PNG. However, what does change is the way in which the statistics of the density field behave.

This owes to the fact that there is now a complete hierarchy of connected correlators of the field. Following the work of [24], and keeping only terms that are linear in f_{NL} , one finds that the next-to-leading-order corrections to the matter power spectrum can be written

$$P(k) = P_{11}(k) + P_{22}(k) + P_{13}(k) + P_{12}(k), \quad (12)$$

where P_{11} is the linear power spectrum and P_{13} and P_{22} are the so-called one-loop corrections, which appear in the standard Gaussian theory [44]. The new term for PNG is P_{12} , which has the form [24]

$$P_{12}(k) = \frac{2D^3(a)f_{\text{NL}}\alpha(k)P_\phi(k)k^3}{7(2\pi)^2} \times \int_{y_{\text{min}}}^{y_{\text{max}}} \frac{dy}{y} y^3 \alpha(yk) P_\phi(yk) \int_{\max[-1, \epsilon_1]}^{\min[+1, \epsilon_2]} d\mu \alpha(k\psi) \times \left(\frac{3y + 7\mu - 10y\mu^2}{1 + y^2 - 2y\mu} \right) \left[1 + \frac{P_\phi(k\psi)}{P_\phi(k)} + \frac{P_\phi(k\psi)}{P_\phi(yk)} \right], \quad (13)$$

where $\psi^2 = k^2(1 + y^2 - 2y\mu)$, $y_{\text{max}} \equiv k_{\text{max}}/k$, and $y_{\text{min}} \equiv k_{\text{min}}/k$. We also defined $\epsilon_1 \equiv [k^2 + q^2 - k_{\text{max}}^2]/2kq$

and $\epsilon_2 \equiv [k^2 + q^2 - k_{\text{min}}^2]/2kq$. The cutoff scales are set to be $k_{\text{max}} = 10 h \text{ Mpc}^{-1}$ and $k_{\text{min}} = 2\pi/L$, with L being the simulation box length. Note that the spectrum P_{12} arises due to the existence of the nonzero primordial potential bispectrum [cf. Eq. (5)].

Let us now define the ratio of the power spectra in the non-Gaussian and Gaussian models as

$$\beta_{\text{PT}}(k, f_{\text{NL}}) \equiv 1 + \frac{P_{12}(k, f_{\text{NL}}, a)}{P_{11}(k, a) + P_{13}(k, a) + P_{22}(k, a)}. \quad (14)$$

In [19] it was shown that, for $k < 0.2 h \text{ Mpc}^{-1}$, the perturbation theory (PT) description was able to capture to high precision the same ratio measured from N -body simulations. In Fig. 2 we extend the analysis to much higher wave numbers, relevant for cosmological weak lensing studies. On the left-hand side of the figure, we show the results for $z = 1.0$ and on the right those for $z = 0.0$ (we provide further details of these measurements in Sec. VI). The top sections of the panels show the absolute power and on a log-log plot the points for the three f_{NL} models cannot be distinguished. The bottom sections show $\beta_{\text{PT}}(k, f_{\text{NL}})$. We see that the effect of $f_{\text{NL}} = \pm 100$ is to induce $\pm \sim 3.5\%$ modulations in the

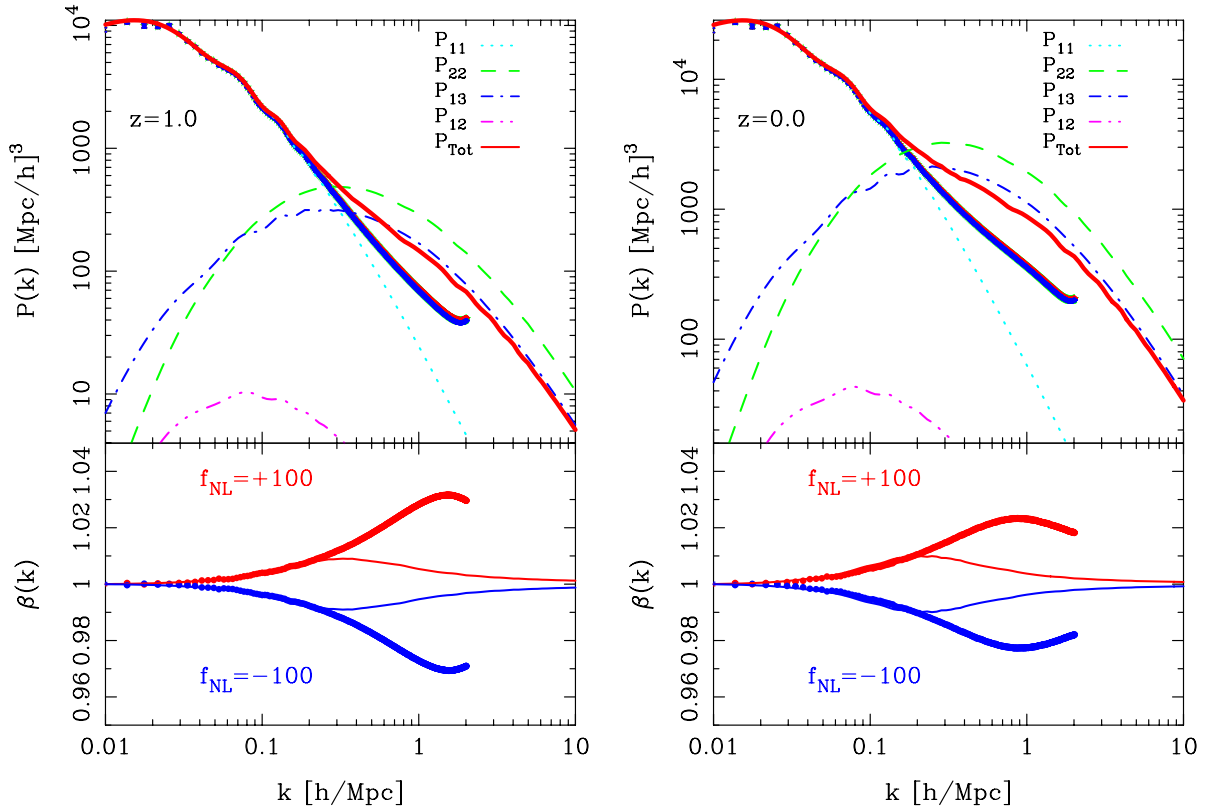


FIG. 2 (color online). Comparison of the nonlinear matter power spectra measured from the suite of N -body simulations with predictions from the nonlinear gravitational perturbation theory. The left and right panels show results for $z = 1.0$ and $z = 0.0$, respectively. The top section of each panel presents the absolute power, and the bottom section shows the ratio of the nonlinear power in the non-Gaussianity to the Gaussian models. Points with errors denote estimates from the simulations, and lines denote theoretical predictions. The colors green, red, and blue denote the models $f_{\text{NL}} = \{0, 100, -100\}$, respectively.

nonlinear matter power spectrum at $z = 1.0$ and on scales of the order of $k = 1.0 h \text{Mpc}^{-1}$ and that this reduces to $\sim 2.5\%$ by $z = 0.0$. These deviations, although small, would be larger than the measurement errors in future weak lensing missions and so need to be accurately characterized.

The figure also shows that, while PT captures well the behavior of β_{PT} measured in the simulations on very large scales $k < 0.2 h \text{Mpc}^{-1}$, it fails to model the results on smaller scales. It is also worth pointing out that while β_{PT} is well characterized for $k < 0.2 h \text{Mpc}^{-1}$, the absolute power does not match well the measured absolute power at that scale, it being a factor of ~ 2 higher than the measurements at $z = 0.0$. This leads us to explore alternative approaches to modeling the nonlinear power spectrum on smaller scales. Before moving on, we note that there are interesting new analytic approaches to solving the perturbation theory at higher orders being developed, i.e. the renormalized perturbation theory and renormalization group theory [45–47]. These will push our analytic understanding deeper into the nonlinear regime $k > 0.2 h \text{Mpc}^{-1}$. However, we point out that the most recent calculations in the literature show only a very modest improvement over the standard PT that we considered in this paper [46]. Moreover, while certainly interesting, these techniques are unlikely to be able to probe the range of wave numbers required for future weak lensing missions ($k \in [0.01, 100.0] h \text{Mpc}^{-1}$).

B. The halo model approach

The halo model was developed by a number of authors [48–50], and for a review see [51]. In this model all of the mass in the Universe is distributed into dark matter haloes, each labeled with some physical properties. Typically one simply labels each halo by its mass; however, more complicated approaches can take into account, for instance, halo shape [43].

In the halo model the density field of dark matter may be written as a sum over all haloes:

$$\rho(\mathbf{x}) = \sum_j^N M_j U_j(\mathbf{x} - \mathbf{x}_j | M_j), \quad (15)$$

where N is the total number of haloes, M_j and \mathbf{x}_j are the mass and center of mass of the j th halo, respectively, and $U_j \equiv \rho_j(\mathbf{x}_j)/M_j$ is the mass normalized density profile. The statistics of the density field may be computed directly. In particular, for the density power spectrum it can be shown that it can be written as the sum of two terms (for more details see [43,52]):

$$P(k) = P_{1\text{H}}(k) + P_{2\text{H}}(k), \quad (16)$$

where the first term is referred to as the “1-halo” term, which describes the intraclustering of dark matter particles within single haloes; the second term is referred to as the

“2-halo” term and describes the clustering of particles in distinct haloes. They have the explicit forms

$$P_{1\text{H}}(k) = \frac{1}{\bar{\rho}^2} \int_0^\infty dM n(M) M^2 |U(k|M)|^2; \quad (17)$$

$$P_{2\text{H}}(k) = \frac{1}{\bar{\rho}^2} \int_0^\infty \prod_{i=1}^2 \{dM_i n(M_i) M_i U_i(k|M_i)\} \times P_{\text{cent}}^{\text{hh}}(k|M_1, M_2), \quad (18)$$

where the essential new ingredient is the power spectrum of halo centers with masses M_1 and M_2 , denoted $P_{\text{cent}}^{\text{hh}}(k|M_1, M_2)$.

C. The halo-center power spectrum

The power spectrum of halo centers contains all of the information for the interclustering of haloes; precise knowledge of this term is required to make accurate predictions on both large and small scales. In principle, $P_{\text{cent}}^{\text{hh}}(k|M_1, M_2)$ is a complicated scale-dependent function of M_1, M_2 , and k [53]. The usual starting point for modeling this is to assume the local deterministic biasing approach [54,55]. This can be summarized as follows. Consider the density field of all haloes with masses in the range M to $M + dM$, smoothed with some filter of scale R . We now assume that this field can be related to the underlying dark matter field, smoothed with the same filter, through some deterministic mapping and that this mapping should apply independently of the precise position \mathbf{x} in the field:

$$\delta^{\text{h}}(\mathbf{x}|R, M) = \mathcal{F}_{\{M,R\}}[\delta(\mathbf{x}|R)], \quad (19)$$

where the subscripts on the function \mathcal{F} indicate that it depends on the mass of the haloes considered and the chosen filter scale. The filtered density field is

$$\delta(\mathbf{x}|R) = \frac{1}{V} \int d^3\mathbf{y} \delta(\mathbf{y}) W(|\mathbf{x} - \mathbf{y}|, R), \quad (20)$$

$W(|x|, R)$ being some normalized filter. Taylor expanding $\mathcal{F}_{\{M,R\}}$ about the point $\delta = 0$ yields

$$\mathcal{F}_{\{M,R\}}[\delta(\mathbf{x}|R)] = \sum_i \frac{b_i(M|R)}{i!} [\delta(\mathbf{x}|R)]^i. \quad (21)$$

We now assume that there is a certain filter scale above which $\mathcal{F}_{\{M,R\}}$ is independent of both the scale considered and also the exact shape of the filter function. Hence,

$$\delta^{\text{h}}(x|R, M) = \sum_{i=0}^\infty \frac{b_i(M)}{i!} [\delta(\mathbf{x}|R)]^i, \quad (22)$$

where the bias coefficients are

$$b_i(M) \equiv \left. \frac{\partial^i \mathcal{F}_{\{M\}}[\chi]}{\partial \chi^i} \right|_{\chi=0}. \quad (23)$$

The bias coefficients from the Taylor series are not independent but obey the constraint $\langle \delta^h(\mathbf{x}|R) \rangle = 0$, which leads to

$$b_0 = -\frac{b_2}{2}\langle \delta^2 \rangle - \frac{b_3}{3!}\langle \delta^3 \rangle - \dots - \frac{b_n}{n!}\langle \delta^n \rangle. \quad (24)$$

Thus, in general b_0 is nonvanishing and depends on the hierarchy of moments. This allows us to rewrite Eq. (22) as

$$\delta^h(x|R, M) = \sum_{i=1}^{\infty} \frac{b_i(M)}{i!} \{[\delta(\mathbf{x}|R)]^i - \langle \delta^i(\mathbf{x}|R) \rangle\}. \quad (25)$$

Nevertheless, we may remove b_0 from further consideration by transforming to the Fourier domain, where it only contributes to $\delta(\mathbf{k} = 0)$.

Thus the halo-center correlation function has the form

$$\begin{aligned} \xi_{\text{hh},R}^{\text{cent}}(r) &\equiv \langle \delta^h(\mathbf{x}|R, M) \delta^h(\mathbf{x} + \mathbf{r}|R, M) \rangle \\ &= b_1(M_1)b_1(M_2)\xi_R(r) + \frac{1}{6}[b_1(M_1)b_3(M_2) \\ &\quad + b_3(M_1)b_1(M_2)]\langle \delta_R(\mathbf{x})\delta_R^3(\mathbf{x} + \mathbf{r}) \rangle \\ &\quad + \frac{b_2(M_1)b_2(M_2)}{4}\langle \delta_R^2(\mathbf{x})\delta_R^2(\mathbf{x} + \mathbf{r}) \rangle + \dots, \end{aligned} \quad (26)$$

where $\xi_R(r)$ is the nonlinear matter correlation function smoothed on scale R . Fourier transforming the above expression we obtain the halo-center power spectrum [53,54,56]:

$$P_{\text{cent}}^{\text{hh}}(k|M_1, M_2) = b_1(M_1)b_1(M_2)P_{\text{NL}}(k|R) + \mathcal{O}(b_2, \dots), \quad (27)$$

where the parameters b_i are the nonlinear bias coefficients and $P_{\text{NL}}(k|R)$ is the nonlinear matter power spectrum smoothed on scale R . It has recently been proposed that, for PNG, the halo bias is also a function of the local gravitational potential [26,57]; we shall not explore this possibility here but simply note that it should give rise to the same scale dependence of the linear bias. Further, since this is a first-order attempt to calculate the effects of PNG on the matter clustering in the halo model, we shall restrict our attention to the case of linear bias and so neglect terms b_i with $i > 1$, whereupon $P_{\text{cent}}^{\text{hh}}$ becomes a separable function of mass and scale. We present details of the $b_1(M, f_{\text{NL}})$ model in Sec. V. For $P_{\text{NL}}(k, R, f_{\text{NL}})$, we make the simple approximation

$$P_{\text{NL}}(k|R, f_{\text{NL}}) = W^2(kR)P_{\text{halofit}}(k)\beta_{\text{PT}}(k, f_{\text{NL}}), \quad (28)$$

where $W(kR)$ is a smoothing function, $P_{\text{halofit}}(k)$ is the nonlinear matter power spectrum model of [58], valid for Gaussian initial conditions, and β_{PT} was defined earlier in Eq. (14).

As was argued in [53,59,60] another essential component of the interclustering of haloes is halo exclusion. That is, one must remove the correlations which arise on scales inside the sum of the virial radii of the two haloes M_1 and

M_2 . As was shown in [53], this effect can formally be written

$$\xi_{\text{cent}}^{\text{hh}}(r|M_1, M_2) = -1 \quad (r < r_{\text{vir},1} + r_{\text{vir},2}), \quad (29)$$

where r_{vir} is the virial radius of a halo and where ξ^{hh} is the correlation function of dark matter halo centers, defined as $\xi_{\text{cent}}^{\text{hh}}(r|M_1, M_2) \equiv \langle \delta^h(\mathbf{x}|M_1)\delta^h(\mathbf{x} + \mathbf{r}|M_2) \rangle$. The -1 in the above is simply the value that ξ must obtain in order for the joint probability of finding halo-center separations $r < r_{\text{vir},1} + r_{\text{vir},2}$ to be zero. In the literature, various approximate schemes have been proposed to model the exclusion effect [59,60]; these involve placing a cutoff in the upper limit of the mass integrals in the 2-halo term. We shall not follow such schemes, since these approaches do not reproduce the correct power spectrum asymptotics for the exact calculation, which we show below. Instead we follow [53] and evaluate the above expression exactly. In this case the halo-center power spectrum can be written in terms of the correlation function of halo centers as

$$P_{\text{cent}}^{\text{hh}}(k|R) = \int d^3\mathbf{r} \xi_{\text{cent}}^{\text{hh}}(k|M_1, M_2, R)j_0(kr). \quad (30)$$

Inserting Eq. (29) for scales inside $r_{\text{vir},1} + r_{\text{vir},2}$ and the relation $\xi_{\text{cent}}^{\text{hh}}(k|M_1, M_2, R) = b(M_1)b(M_2)\xi(r|R)$ on larger scales, where $\xi(r|R)$ is the dark matter correlation function smoothed on the scale R , we find

$$\begin{aligned} P_{\text{cent}}^{\text{hh}}(k|R) &= \int_{r_{\text{vir},1} + r_{\text{vir},2}}^{\infty} d^3\mathbf{r} b(M_1)b(M_2)\xi(r|R)j_0(kr) \\ &\quad + \int_0^{r_{\text{vir},1} + r_{\text{vir},2}} d^3\mathbf{r} (-1)j_0(kr) \\ &= \int_0^{\infty} d^3\mathbf{r} b(M_1)b(M_2)\xi(r|R)j_0(kr) \\ &\quad - \int_0^{r_{\text{vir},1} + r_{\text{vir},2}} d^3\mathbf{r} [1 + b(M_1)b(M_2)\xi(r|R)]j_0(kr) \\ &= P_{\text{cent}}^{\text{NoExc, hh}}(k) - P_{\text{cent}}^{\text{Exc, hh}}(k). \end{aligned} \quad (31)$$

The first term in the last line of the above equation represents the usual expression for the clustering of halo centers, and the second term represents the correction due to halo exclusion:

$$P_{\text{cent}}^{\text{NoExc, hh}} \equiv b(M_1)b(M_2)P_{\text{Lin}}(k); \quad (32)$$

$$P_{\text{cent}}^{\text{Exc, hh}} \equiv \int_0^{r_{\text{vir},1} + r_{\text{vir},2}} d^3\mathbf{r} [1 + b(M_1)b(M_2)\xi(r)]j_0(kr). \quad (33)$$

Taking $s \equiv s(M_1, M_2) \equiv r_{\text{vir},1} + r_{\text{vir},2}$ and $y \equiv ks$, we may deduce the following asymptotic properties for $P_{\text{cent}}^{\text{Exc, hh}}$:

- (i) *Large-scale limit.*—For the case $k \rightarrow 0$, we have that $j_0(kr) \rightarrow 1$ and so

$$\begin{aligned} \lim_{y \rightarrow 0} P_{\text{cent}}^{\text{exc, hh}}(k|M_1, M_2) &= \int_0^s d^3\mathbf{r} [1 + b(M_1)b(M_2)\xi(r)] \\ &= V(s)[1 + b(M_1)b(M_2)\bar{\xi}(s)], \end{aligned} \quad (34)$$

where $V(s) = 4\pi s^3/3$ is the volume of the exclusion sphere for the haloes M_1 and M_2 and where $\bar{\xi}$ is the volume averaged correlation function. This appears as a white noise power contribution, and so it acts to reduce any large-scale shot-noise component.

(ii) *Small-scale limit.*—For the case $k \rightarrow \infty$, we have that

$$\begin{aligned} \lim_{k \rightarrow \infty} P_{\text{cent}}^{\text{exc, hh}}(k|M_1, M_2) &= \lim_{k \rightarrow \infty} \int_0^s d^3\mathbf{r} [1 + b(M_1)b(M_2)\xi(r)] j_0(kr) \\ &= \lim_{k \rightarrow \infty} \left\{ \frac{1}{k^3} \int_0^{ks} d^3\mathbf{y} j_0(y) \right\} \\ &\quad + \lim_{k \rightarrow \infty} \left\{ \frac{1}{k^3} \int_0^{ks} d^3\mathbf{y}' b(M_1)b(M_2)\xi(y'/k) j_0(y') \right\} \\ &= (2\pi)^3 \delta^D(\mathbf{k}) + P_{\text{cent}}^{\text{NoExc, hh}}(k). \end{aligned} \quad (35)$$

Thus the effect of halo exclusion on small scales is to exactly null the 2-halo term without exclusion.

This leads us to write the full 2-halo term as $P_{2\text{H}}(\mathbf{k}) - P_{2\text{H}}^{\text{exc}}(\mathbf{k})$, where

$$\begin{aligned} P_{2\text{H}}^{\text{exc}}(k) &= \frac{1}{\bar{\rho}^2} \int_0^\infty \prod_{l=1}^2 \{dM_l n(M_l) M_l U_l(\mathbf{k}|M_l)\} \\ &\quad \times \int_0^{r_{\text{vir},1} + r_{\text{vir},2}} d^3\mathbf{r} [1 + b(M_1)b(M_2)\xi(r)] j_0(kr). \end{aligned} \quad (36)$$

As a short aside, in Appendix B we forward the idea that halo exclusion may resolve the well known problem of excess large-scale power in the standard formulation of the halo model and that after taking this into account the theory is consistent with perturbation theory results, like the renormalized perturbation theory (RPT) [61].

V. HALO MODEL INGREDIENTS IN NON-GAUSSIAN MODELS

The model that we described in Sec. IV B specified nothing about the cosmological model, other than that the end state of gravitational clustering leads to the formation of a distribution of haloes with some characteristic spectrum of masses and density profiles and that halo centers are clustered. Thus no extension of the formalism is necessary in order to use the halo model to describe clustering in more exotic models, such as PNG. However, what must necessarily change are the ingredients of the model: the mass function, the halo bias, and the density

profiles. We now study these in detail in the context of PNG.

A. The halo mass function

The mass function of dark matter haloes in models of structure formation from Gaussian initial conditions has been widely studied over the past decades [62–67]. Conventionally, the mass function is represented

$$\frac{dn}{d \log M} = \frac{\bar{\rho}}{M} f(\nu) \frac{d \log \nu}{d \log M}; \quad \nu \equiv \frac{\delta_c(z)}{\sigma(M)}, \quad (37)$$

where for the Press-Schechter (PS) and Sheth and Tormen (ST) mass function we have, respectively,

$$f_{\text{PS}}(\nu) = \sqrt{\frac{2}{\pi}} \nu \exp\left[-\frac{\nu^2}{2}\right]; \quad (38)$$

$$f_{\text{ST}}(\nu) = A \sqrt{\frac{2}{\pi}} \sqrt{q} \nu [1 + (\sqrt{q} \nu)^{-2p}] \exp\left[-\frac{q \nu^2}{2}\right]. \quad (39)$$

For the ST mass function the amplitude parameter A is determined from the constraint $\int d \log \nu f(\nu) = 1$, which leads to $A^{-1} = \{1 + 2^{-p} \Gamma[0.5 - p] / \Gamma[0.5]\}$. ST's original parameters are $\{A = 0.3222, p = 0.3, q = 0.707\}$. The derivative term on the right-hand side can be calculated from Eq. (A8) in Appendix A. Figure 1 shows the derivative of Eq. (A8) computed for the WMAP5 parameters compared to the skewness due to PNG.

A number of authors have studied the effects of PNG of the local type on the mass function of dark matter haloes [13, 18, 20, 21, 68–70]. The most important task in extending the Press-Schechter framework is to find an analytic expression for the 1-point probability density function (PDF) of the smoothed matter fluctuations. Matarrese, Verde, and Jimenez [13] [hereafter MVJ] gave the first formal derivation using a path-integral approach. Lo Verde *et al.* [68] [hereafter LV] used the Edgeworth expansion (or more simply the Gram-Charlier type Ia series) to recover the PDF. The key idea of these expansions is to write the characteristic function of the non-Gaussian PDF to be approximated in terms of the characteristic function of the Gaussian PDF and to then recover the non-Gaussian PDF through the inverse Fourier transform method (see [71]).

For small amounts of PNG the mass function can be written

$$\frac{dn(M f_{\text{NL}})}{d \log M} = \frac{dn_{\text{ST}}(M)}{d \log M} R(\nu, f_{\text{NL}}), \quad (40)$$

where the ratio of the non-Gaussian to the Gaussian mass functions of MVJ and LV can be written

$$\begin{aligned}
 R_{\text{MVJ}}[\nu, f_{\text{NL}}] &= \exp\left[\frac{\tilde{\delta}_c^3(a)S_3(M, a_0)}{6\sigma^2(M, a_0)}\right] \\
 &\times \left| \frac{1}{6} \frac{\tilde{\delta}_c(a)}{\sqrt{1 - \tilde{\delta}_c(a)S_3(M, a_0)/3}} \frac{dS_3(M, a_0)}{d \log \sigma} \right. \\
 &\left. + \sqrt{1 - \frac{1}{3} \tilde{\delta}_c(a)S_3(M, a_0)} \right|, \quad (41)
 \end{aligned}$$

$$\begin{aligned}
 R_{\text{LV}}[\nu, f_{\text{NL}}] &= 1 + \frac{1}{6} \sigma(M|a_0)S_3(M|a_0)[\tilde{\nu}^3(a) - 3\tilde{\nu}(a)] \\
 &+ \frac{1}{6} \frac{d[\sigma(M|a_0)S_3(M|a_0)]}{d \log \sigma} \left[\tilde{\nu}(a) - \frac{1}{\tilde{\nu}(a)} \right], \quad (42)
 \end{aligned}$$

where in the above equations $\tilde{\nu} \equiv \tilde{\delta}_c(a)/\sigma(M, a_0)$ and where we use the rescaled linear collapse density: $\tilde{\delta}_c(a) = \sqrt{q}\delta_c/D(a)$. In the spherical collapse model, the linearly

extrapolated density threshold for collapse is $\delta_c = 1.686$. Note that, as in the Press-Schechter formalism, we have chosen to evaluate the variance and the skewness of the density field at the present time a_0 and in so doing have transferred the time dependence of the theory to the collapse barrier $\delta_c(a) = \delta_c(a_0)/D(a)$.

Note that these formulas are not the same as those originally derived by MVJ and LV but differ by the \sqrt{q} in the definition of the peak height. This was introduced by Grossi *et al.* in a heuristic way in order to obtain a good fit to the FoF mass functions in their numerical simulations. They conjecture that it appears for the same reason as it appears in the ST mass function [see also [69]]. The true origins for such a factor are unclear, since for the case of haloes identified through a bound spherical overdensity criterion no q correction is required [19].

Figure 3 compares the mass function of FoF ($b = 0.2$) dark matter haloes measured from the ensemble of simulations at redshifts: $z \in [1.0, 0.5, 0.28, 0.0]$. The left and right panels compare the simulation estimates with the

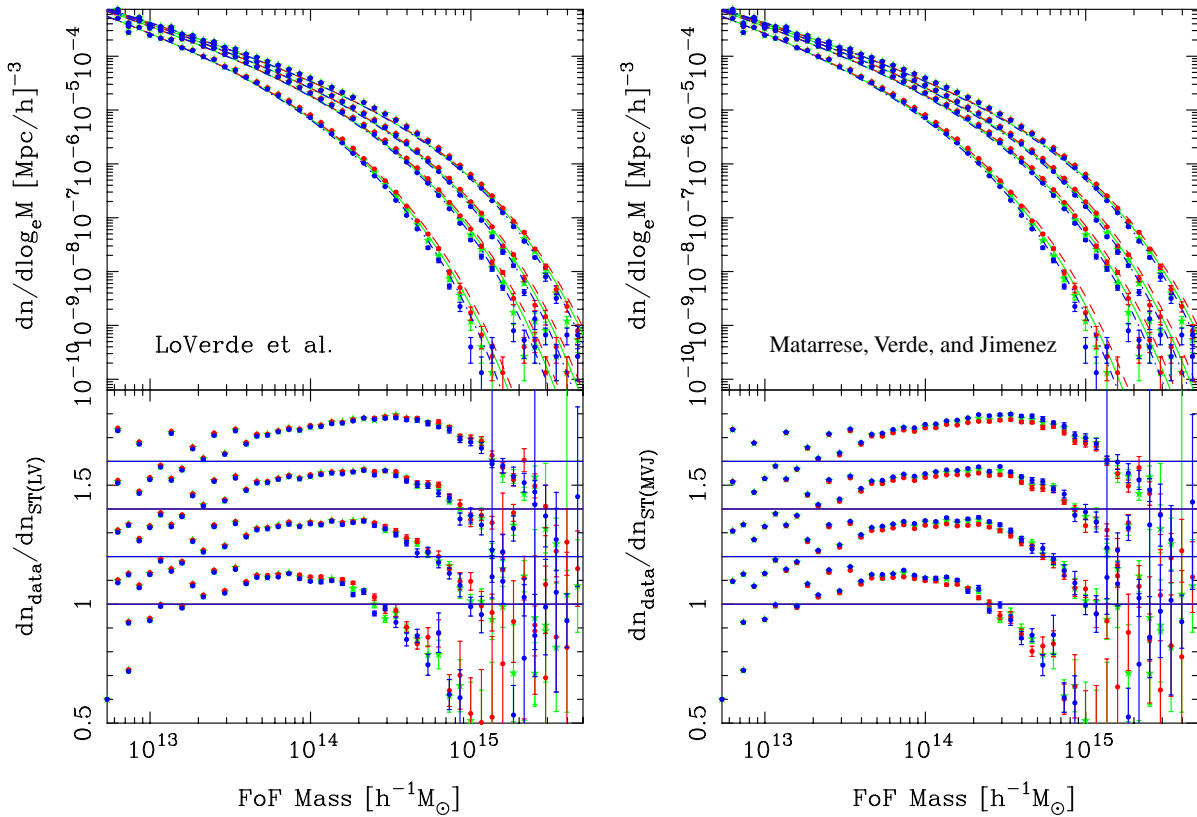


FIG. 3 (color online). Mass functions of haloes in models with local primordial non-Gaussianity as a function of FoF ($b = 0.2$) halo mass and at several redshifts. Left and right panels compare estimates from the ensemble of N -body simulations with the theoretical predictions of Lo Verde *et al.* [68] and Matarrese, Verde, and Jimenez [13], respectively. Gaussian mass function predictions are given by Sheth and Tormen [62]. Top panels show the absolute mass function. The green, red, and blue points with errors denote estimates for $f_{\text{NL}} = \{0, +100, -100\}$, respectively. The solid, dashed, and dot-dashed lines represent the predictions as given by Eq. (40) for $f_{\text{NL}} = \{0, 100, -100\}$, respectively. From bottom to top the points show results for redshifts $z \in \{1.0, 0.5, 0.28, 0.0\}$. Bottom panels: Ratio of the estimated mass functions with their respective theoretical predictions. For clarity, we have offset the results for redshifts $z \in \{1.0, 0.5, 0.28, 0.0\}$ by $\{0.0, 0.2, 0.4, 0.6\}$ in the positive y direction.

predictions from the LV and MVJ models, respectively. The top panels show the absolute mass function and bottom panels show the ratio with respect to the theory. In these plots we take the Gaussian model for the mass function to be that as given by [62]. Note that the errors on the points show the error on the mean, i.e. the box-to-box variance divided by the square root of the number of realizations: $\sigma/\sqrt{N_{\text{ensem}}} \sim \sigma/3.5$.

A number of important points may be noted. First, none of these models fit the data well [26]; however, this can be mainly attributed to the fact that the ST mass function does not fit well the Gaussian simulation data: We see a $\sim 10\%$ – 20% excess in the number of intermediate-mass haloes $M_* < M < 100M_*$ and strong suppression in the numbers of high-mass haloes $M > 100M_*$. Second, we note that, as expected, the model with $f_{\text{NL}} > 0$ ($f_{\text{NL}} < 0$) produces an excess (reduction) in the number of high-mass haloes relative to the Gaussian case. The predictions capture these trends. However, as can be seen from the lower section of the left figure, the model of LV produces the same locus of points for all of the models $f_{\text{NL}} \in [\pm 100, 0]$ and for all redshifts, whereas that of MVJ, being almost equally as good, produces a slightly different offset for each f_{NL} model and at different redshifts. This leads us to conclude that in order to accurately predict the mass function in non-Gaussian models over a wide range of masses and redshifts, one simply requires an accurate fit to the Gaussian model, combined with the ratio model of LV.

Figure 4 further emphasizes this point. Here we show the fractional mass function for the FoF dark matter haloes measured in the simulations at the four expansion factors. For each simulation we compute the mass function of haloes and take the ratio of this estimate with respect to the Gaussian model. These results are averaged over the 12

realizations and the errors are computed on the mean. On comparing these estimates with the theoretical predictions from the models of LV and MVJ we find excellent agreement when the shift parameter $\delta_c \rightarrow \sqrt{q}\delta_c$ is used, as advocated in [20]. There is a small preference to the model of LV, especially at late times for high-mass haloes in the model with $f_{\text{NL}} = 100$. Coupled with the fact that the mass function ratios with respect to the ST + LV model are well behaved, we shall hereafter adopt the LV model for all our halo model calculations.

Finally, we note that the ST mass function is preferred over other commonly used expressions such as that of [65], since it obeys the important property that when integrated over all masses, one recovers the mean matter density.

B. Halo bias

The halo model also requires us to specify how the centers of dark matter haloes of different masses cluster with respect to each other. As described by Eq. (27), for the Gaussian model, and at first order in the dark matter density, halo and matter density perturbations can be related through a scale-independent bias factor $b(M)$. Following [56,62], an application of the peak-background split approximation enables one to calculate $b(M)$ from a given mass function. For the ST mass function the Gaussian bias has the form

$$b_{\text{ST}}(\nu) = 1 + \frac{q\nu^2 - 1}{\delta_c(z)} + \frac{2p}{1 + (q\nu^2)^p}; \quad (43)$$

$$\nu \equiv \frac{\delta_c(z)}{\sigma(M, z=0)},$$

where the parameters $\{p, q\}$ are as in Eq. (39).

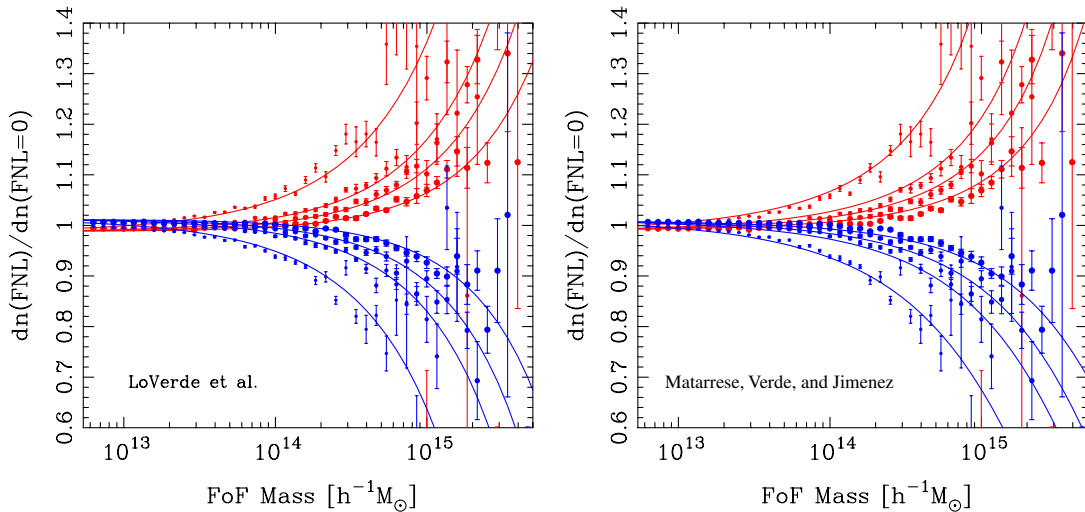


FIG. 4 (color online). Ratio of the non-Gaussian to Gaussian mass functions as a function of FoF ($b = 0.2$) halo mass. Left and right panels show compare the simulations with the theoretical models of [13,68], respectively. The points with errors denote the ensemble averages of the mass function ratios measured at expansion factors $z \in [1.0, 0.5, 0.28, 0.0]$, where larger point symbols denote later times. Solid lines denote theoretical models. The theory predictions were generated using $\delta_c \rightarrow \sqrt{q}\delta_c$.

As was summarized in [19], with PNG there are two main effects on the bias. First, local non-Gaussianity induces a scale-dependent correction factor on extremely large scales $k < 0.02 h \text{Mpc}^{-1}$ [18,23,26]. Second, assuming that the peak-background split holds, then there is also a scale-independent correction to the bias. This arises due to the fact that the mass function changes with f_{NL} and consequently the typical halo mass changes and hence the bias [22,72]. Thus the non-Gaussian bias may be written

$$b_{\text{NG}}(k, M, f_{\text{NL}}) = b_{\text{G}}(M) + \Delta b_{\kappa}(k, M, f_{\text{NL}}) + \Delta b_{\text{I}}(M, f_{\text{NL}}). \quad (44)$$

The scale-dependent bias term $\Delta b_{\kappa}(k, M, f_{\text{NL}})$ can be written

$$\Delta b_{\kappa}(k, M, a) \equiv 2f_{\text{NL}}[b_{\text{G}}(M, a) - 1] \frac{3\Omega_m H_0^2 \delta_c(a)}{2D(a)c^2 T(k)k^2}. \quad (45)$$

In the original derivation of [18], as was pointed out by Matarrese and Verde [23], a factor of the transfer function was missing, and it has been added in the above expression. Furthermore, in the original derivation one sees that the term in brackets involves just the Gaussian bias $b_{\text{G}}(M, a)$. However, as we will show in Eq. (56), this should in fact be the sum of the Gaussian bias and the scale-independent bias correction due to PNG.

The scale-independent bias correction Δb_{I} can be written

$$\Delta b_{\text{I}} = -\frac{1}{\sigma} \frac{\partial \ln[R(\nu, f_{\text{NL}})]}{\partial \nu}, \quad (46)$$

where R is the fractional correction to the mass function. For the case of Lo Verde *et al.* [68] the scale-independent bias has the form

$$\Delta b_{\text{I}}^{\text{LV}} = -\frac{1}{6\sigma R_{\text{LV}}} \left[-\frac{d^2(\sigma S_3)}{d \ln \nu^2} \left(1 - \frac{1}{\nu^2}\right) + \frac{d(\sigma S_3)}{d \ln \nu} \left(\nu^2 - 4 - \frac{1}{\nu^2}\right) + 3\sigma S_3(\nu^2 - 1) \right]. \quad (47)$$

It is worth noticing that $\Delta b_{\text{I}}(f_{\text{NL}})$ has a sign opposite to that of f_{NL} (because the bias decreases when the mass function goes up).

The scale dependence of the above non-Gaussian bias model, for haloes with masses above $M \sim 10^{13} h^{-1} M_{\odot}$, was recently tested against a suite of high-resolution N -body simulations by [19–21]. For the cross-power spectrum of haloes and matter, it was shown to work at a precision of better than 10%. However, the form of the bias has not been investigated for halo masses substantially lower than M^* . In order to make a halo model calculation for the mass power spectrum one is required to average over haloes of all masses and so it is important to understand the behavior for $\nu < 1$ as well as for $\nu > 1$. Note that while the mass function of [68] should only be trusted for $\nu \geq 1$ and hence also the bias expansion, since we see no

deviations at $\nu \sim 1$ we shall assume that these expansions can be trusted to lower ν .

In Fig. 5, using Eqs. (47) and (45), we show how the halo bias depends on halo mass, and we extrapolate these relations to masses $M/M_* \leq 1$ [note that in evaluating the scale-independent bias we have made the approximation $d^2(\sigma S_3)/d \ln \nu^2 = 0$]. Since the bias is also scale-dependent, we show the results for spatial scales $k \in \{0.005, 0.05\} h \text{Mpc}^{-1}$.

On very large scales $k \sim 0.005 h \text{Mpc}^{-1}$ (left panel in Fig. 5), we see that the scale-dependent bias correction Δb_{κ} strongly modulates the Gaussian bias, increasing (decreasing) the bias of high-mass haloes for $f_{\text{NL}} > 0$ ($f_{\text{NL}} < 0$). For low-mass haloes with $\nu < 1$ this trend reverses. On smaller scales $k \sim 0.005 h \text{Mpc}^{-1}$ (right panel in Fig. 5), the scale-dependent bias has been strongly suppressed and the scale-independent term starts to dominate. The consequence of this is that high-mass haloes in models with $f_{\text{NL}} > 0$ ($f_{\text{NL}} < 0$) have a slightly lower (higher) bias than in the Gaussian case. Again this trend is reversed for haloes with $\nu < 1$.

In evaluating the 2-halo term we must compute integrals of the type as given in Eq. (18). If we consider again the large-scale limit $U(k|M, f_{\text{NL}}) \rightarrow 1$ as $k \rightarrow 0$, then this places the following conditions on the Gaussian and non-Gaussian mass functions and bias:

$$\int dMM n_{\text{G}}(M) b_{\text{G}}(M) = \bar{\rho}; \quad (48)$$

$$\int dMM n_{\text{NG}}(M) b_{\text{NG}}(M) = \bar{\rho}. \quad (49)$$

These relations arise simply from the fact that

$$\bar{n}(\mathbf{x}, M) = \bar{n}(M)[1 + \delta^{\text{h}}(\mathbf{x}|M)]. \quad (50)$$

Taking the nonlinear local bias model of [54] for the halo density field, $\delta^{\text{h}}(\mathbf{x}|M) = \sum_{i=0}^{\infty} b_i(M) \delta^i(\mathbf{x})/i!$, and on integrating Eq. (50) over all haloes, weighted by the mass, we must recover the mass density field:

$$\begin{aligned} \bar{\rho}[1 + \delta(\mathbf{x})] &= \int_0^{\infty} dMM \bar{n}(M)[1 + \delta^{\text{h}}(\mathbf{x}|M)] \\ &= \int_0^{\infty} dMM \bar{n}(M) \left[1 + \sum_{i=0}^{\infty} \frac{b_i(M)}{i!} \delta^i(\mathbf{x}) \right]. \end{aligned} \quad (51)$$

The integral resulting from the first term in the bracket on the right side gives us the normalization condition for the mass function $\int_0^{\infty} dMM \bar{n}(M) = \bar{\rho}$, and the integral of the second term gives

$$\delta(\mathbf{x}) = \frac{1}{\bar{\rho}} \int_0^{\infty} dMM \bar{n}(M) \sum_{i=0}^{\infty} \frac{b_i(M)}{i!} \delta^i(\mathbf{x}). \quad (52)$$

This can only be true if and only if Eqs. (48) and (49) are true. As a caveat we also note the further condition

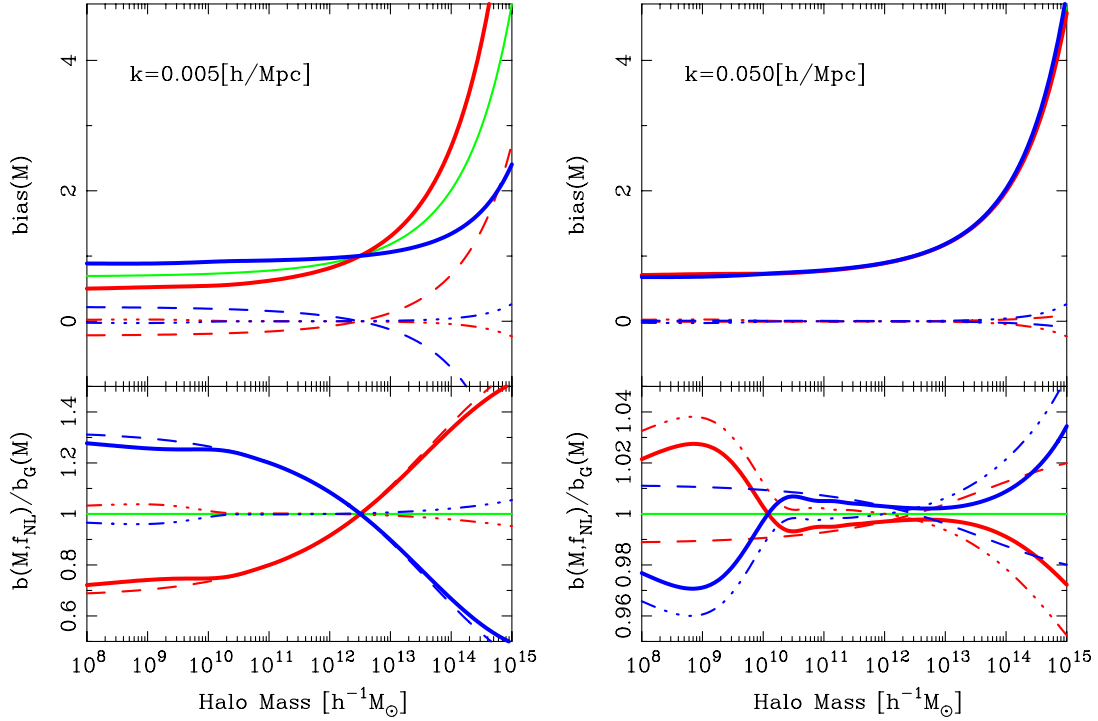


FIG. 5 (color online). Mass dependence of halo bias in models with primordial non-Gaussianity. The left and right panels show results for the halo bias on scales $k = \{0.005, 0.05\} h \text{ Mpc}^{-1}$, respectively. Top panels: Absolute bias vs halo mass. The green, red, and blue lines correspond to the cases $f_{\text{NL}} = \{0, 100, -100\}$, respectively; dashed lines denote the scale-dependent contribution $\Delta b_\kappa(k, f_{\text{NL}})$; and triple-dot-dashed lines denote the scale-independent contribution Δb_l . Bottom panels show the ratio of the non-Gaussian bias to the Gaussian bias. Solid lines denote the bias ratio for the sum of all components; dashed lines denote the same but excluding the scale-independent bias; triple-dot-dashed lines denote the same but excluding the scale-dependent bias.

$$\int dM M n(M) b_i(M) = 0 \quad (i \neq 1). \quad (53)$$

Following Eq. (49), for PNG this implies the further two conditions that

$$\int dM M n_{\text{NG}}(M) [b_G(M) + \Delta b_l(M|f_{\text{NL}})] = \bar{\rho}, \quad (54)$$

$$\int dM M n_{\text{NG}}(M) \Delta b_\kappa(k, M|f_{\text{NL}}) = 0. \quad (55)$$

The last condition can only be correct if b_G in Eq. (45) becomes $b_G + \Delta b_l$, i.e.

$$\Delta b_\kappa(k, M) \equiv f_{\text{NL}} [b_G(M) + \Delta b_l(M) - 1] \frac{3\Omega_m H_0^2 \delta_c}{D c^2 T(k) k^2}. \quad (56)$$

This correction has not been pointed out in any previous work and we expect it to affect the scale dependence of the bias. We note that this should also lead to a small asymmetry between the predictions for $f_{\text{NL}} > 0$ and those for $f_{\text{NL}} < 0$.

Returning to the halo model given Eq. (55) and the fact that as k becomes larger Δb_κ becomes less important (cf. Fig. 5), we make the approximation for the dark matter that $\Delta b_\kappa = 0$ on all scales. For an alternative approach to imposing Eq. (55) see [31].

C. Halo density profiles

1. Gaussian profiles

The density profiles of dark matter haloes in simulations evolving from Gaussian initial conditions have been studied in great detail. A reasonably good approximation for the spherically averaged density profile is the Navarro, Frenk, and White (NFW) model [73]. This can be written

$$\rho_{\text{NFW}}(r|M) = \bar{\rho} \delta_c(M) \left[\frac{r}{r_0} \left(1 + \frac{r}{r_0} \right)^2 \right]^{-1}, \quad (57)$$

where the two parameters are the scale radius r_0 and the characteristic density δ_c . Note that if we define the halo mass to be $M_{\text{vir}} = 4\pi r_{\text{vir}}^3 200\bar{\rho}/3$, then owing to mass conservation there is only one free parameter, the concentration parameter $c(M) \equiv r_{\text{vir}}/r_0$, and we have

$$\delta_c(M) = \frac{200c^3/3}{\log(1+c) - c/(1+c)}. \quad (58)$$

The parameter $c(M)$ can be obtained from the original model of NFW, but instead we prefer to use the model of Bullock *et al.* [74]. Note that we correct $c(M)$ for the fact

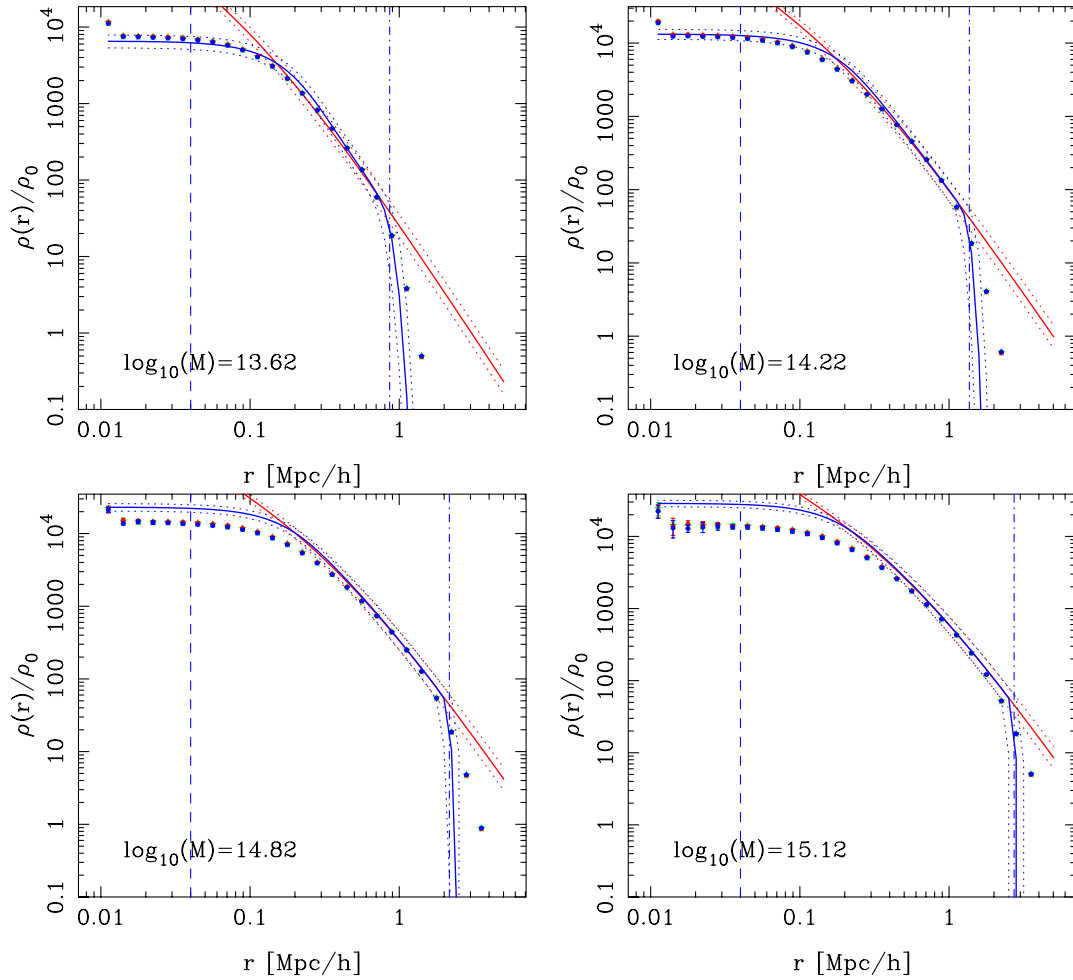


FIG. 6 (color online). Ensemble average density profiles of the dark matter haloes in the Gaussian ($f_{\text{NL}} = 0$) simulations as a function of radius. The panels show haloes with bin centered masses $\log_{10}(M)/h^{-1}M_{\odot} \in \{13.62, 14.22, 14.92, 15.42\}$. In all panels, points with errors show estimates from the simulations; red solid lines give the results for the NFW model; blue solid lines give results for NFW model convolved with a Gaussian filter of radius 2.5 times the softening scale. The dotted lines either side of the main prediction give the predictions if the halo mass associated with the upper and lower edges of the mass bin is used. Vertical dashed lines denote the softening length and vertical dot-dashed curves denote r_{vir} for the central mass of the bin. Note that the density profiles are constructed from only those particles that are members of the FoF groups.

that the definitions of the virial radius in the Bullock *et al.* model and the Sheth and Tormen mass definition used for the mass function are different (for details as to how to do this see [43]). Over the past decade a number of alternative models for halo profiles have emerged. Owing to the relatively low resolution of our haloes we believe that the original model of NFW will be of sufficient accuracy to describe our haloes.

Figure 6 shows the ensemble average density profiles of dark matter haloes in the simulations. The haloes were separated into a set of mass bins of equal logarithmic width $\Delta \log_{10} M = 0.3$ and with the minimum halo mass from which a profile can be estimated being taken as 50 particles ($M \sim 1.5 \times 10^{13} h^{-1} M_{\odot}$). Note that, while the number of particles is relatively small for the lowest mass haloes used in the profile estimation, as Table I shows, we are averaging

TABLE I. The expected number of haloes in the mass bins from which density profile averages are calculated, per simulation. Columns are (1) number of mass bins; (2)–(3) lower and upper edges of the mass bin; (4)–(6) number of haloes in bin.

Bin #	$\log_{10} M_1 [h^{-1} M_{\odot}]$	$\log_{10} M_2 [h^{-1} M_{\odot}]$	# haloes $f_{\text{NL}} = 0$	# haloes $f_{\text{NL}} = 100$	# haloes $f_{\text{NL}} = -100$
1	13.169	13.469	617 526.6	613 869.9	620 691.9
2	13.469	13.769	311 273.1	309 856.2	312 781.2
3	13.769	14.069	144 713.0	144 526.5	144 994.3
4	14.069	14.369	60 805.3	61 050.2	60 481.0
5	14.369	14.669	21 744.9	22 108.4	21 371.4
6	14.669	14.969	5843.5	6080.4	5608.2
7	14.969	15.269	1008.0	1092.5	922.5
8	15.269	15.369	86.7	101.1	72.7

over large numbers of haloes and multiple simulations per mass bin. The figure shows the results for a subsample of four of the mass bins, and these correspond to bins $\{2, 4, 6, 7\} = \{13.62, 14.22, 14.92, 15.12\}[\log_{10}M/h^{-1}M_{\odot}]$ in Table I.

We estimate the density profile for each individual halo by taking only the particles that are in the FoF halo ($b = 0.2$). We compute the halo center of mass and the radial distance of each particle from this center. The particles are then binned into equal logarithmic radial bins of thickness $\Delta \log_{10}r[h^{-1}\text{Mpc}] = 0.1$. Our estimate for the profile is then given by $\hat{\rho}(r_i, \bar{M}) = m_p N_{ij}[r_i, \bar{M}_j]/V_{\text{shell}}(r)$, where $N_{ij}[r_i, \bar{M}_j]$ is the number of particles in the i th radial bin for haloes in mass bin \bar{M}_j and the shell volume is $V_{\text{shell}} = 4\pi[(r_i + \Delta r_i/2)^3 - (r_i - \Delta r_i/2)^3]/3$.

In Fig. 6 we see that the model and the data do not agree at the inner and outer parts of the profile. The data are

significantly flatter in the inner radius than the NFW model would suggest. However, the softening length for the simulations was $r \sim 0.04 h^{-1}\text{Mpc}$, and so at this scale we expect the core to be effectively of constant density. The vertical dashed line in each plot shows the softening length. The virial radius taken as r_{vir} is plotted for the mean mass in the bin and this is the vertical dot-dashed line in each panel. There is reasonable agreement between the scale at which the FoF haloes are truncated and r_{vir} .

We considerably improve the agreement between the NFW model and the data by convolving the theoretical profiles with a Gaussian filter function of radius 2.5 times the softening length, i.e.

$$\tilde{\rho}_{\text{NFW}}(r|M) = \int \frac{d^3\mathbf{k}}{(2\pi)^3} M U_{\text{NFW}}(k|M) W(k) j_0(kr), \quad (59)$$

where $W(k) \equiv \exp[-(2.5l_{\text{soft}}k)^2/2]$ and where $U(r|M) \equiv \rho(r|M)/M$ is the mass normalized profile. We truncate the

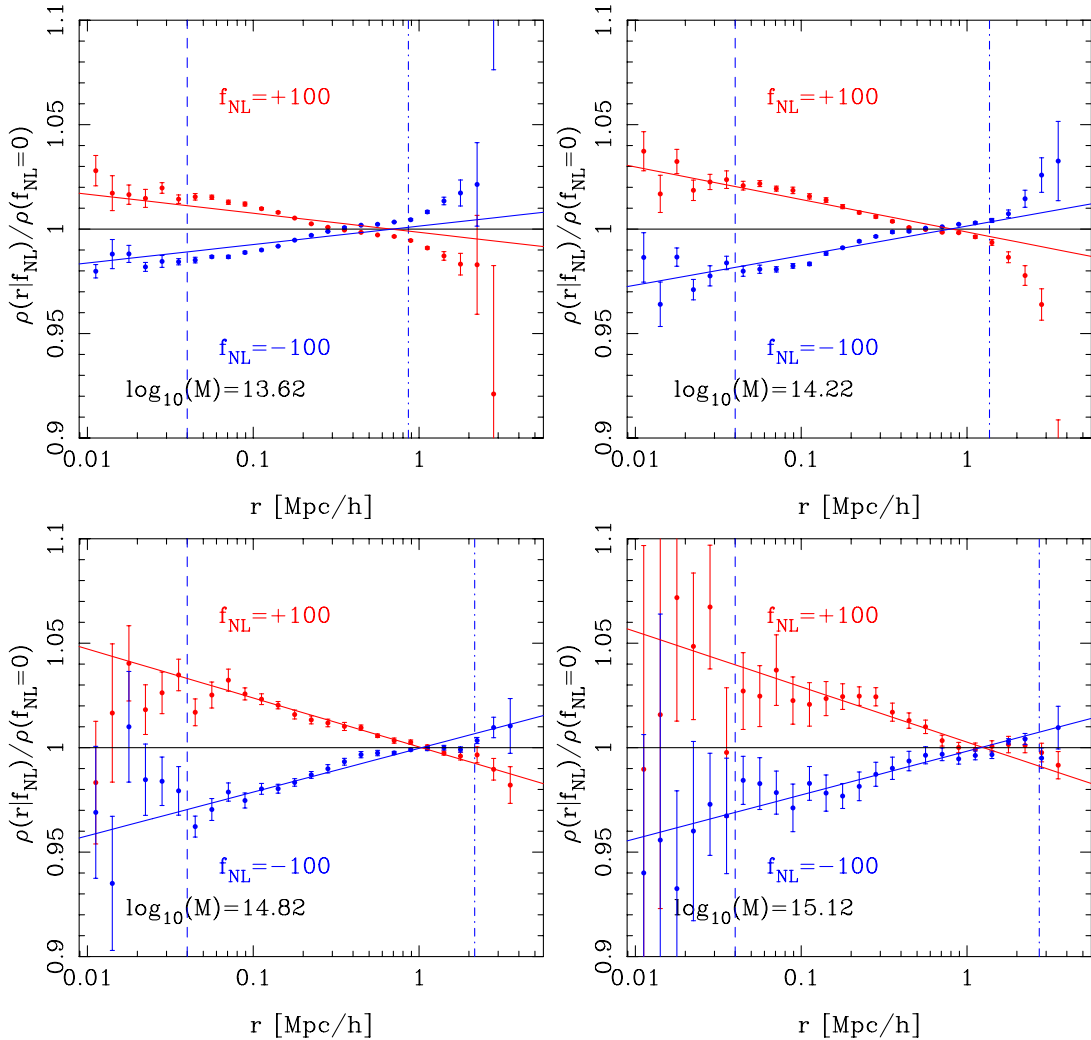


FIG. 7 (color online). Ensemble average of the ratio of the density profiles in the non-Gaussian model with the profiles in the non-Gaussian models as a function of radius. The red and blue colors corresponding to $f_{\text{NL}} = 100$ and $f_{\text{NL}} = -100$, respectively. The points with errors denote estimates from the simulations; solid lines denote the log-linear profile ratio model as given by Eq. (61), and the vertical lines are as in Fig. 6.

profile at the virial radius and for the NFW model the Fourier transform can be written as [51]

$$\begin{aligned}
 f(c)U_{\text{NFW}}(k|M) = & -\frac{\sin(kcr_0)}{kr_0(1+c)} + \cos[kr_0(1+c)] \\
 & \times \{C_i[kr_0(1+c)] - C_i[kr_0]\} \\
 & + \sin[kr_0(1+c)] \\
 & \times \{S_i[kr_0(1+c)] - S_i[kr_0]\}, \quad (60)
 \end{aligned}$$

where $f(c) \equiv [\log(1+c) - c/(1+c)]$ and where S_i and C_i are the standard sine and cosine integrals, respectively. This makes the agreement between the low-mass halo samples and the data almost perfect; however, the higher mass halo samples would require larger smoothing radii to explain the difference. One might motivate this by the fact that for the highest mass bins these haloes are just forming and as such are more likely to have complex structure, so the center of mass may not be a good proxy for the halo center. A better choice may be the point of deepest potential. We shall not pursue this matter further, but note that for the highest mass haloes in our simulations the profiles appear to be flatter inside $r \sim 0.5 h^{-1} \text{Mpc}$.

2. Primordial non-Gaussianity and density profiles

The impact of PNG on the density profiles of dark matter haloes has not been investigated previously. We therefore make a short exploration.

Figure 7 shows the ratio of the density profiles in the non-Gaussian simulations with those from the Gaussian ones. We estimate this quantity by dividing the mean halo profile for each mass bin for each f_{NL} simulation with the corresponding one from the Gaussian runs. The plotted points with errors are then the average and $1-\sigma$ errors from the 12 simulations. In the figure we clearly see that there is an effect of PNG on the profiles. For the case of $f_{\text{NL}} > 0$, we find that the profiles are denser in the inner regions of the halo; the converse is true for the case $f_{\text{NL}} < 0$. For $f_{\text{NL}} = \pm 100$, the strength of the effect depends on the halo mass considered: For cluster-, group-, and small-group-mass haloes we find effects of the order of $\{\lesssim \pm 4.5\%, \pm \lesssim \pm 3.5\%, \lesssim \pm 2.5\%\}$.

Since the power spectrum in the halo model depends on both the profile and the square of the profile, these effects are important to characterize for accurate clustering predictions on small scales. We therefore attempt to model this in a simple way. From Fig. 7 it can be seen that the profile ratio as a function of log radius appears to be almost a straight line. We therefore fit a log-linear model to the measured profile ratios. Explicitly the ratio model has the form

$$R_\rho(r, M, f_{\text{NL}}) - 1 = m \log_{10}[r/r_X], \quad (61)$$

where m is the change in the slope and r_X is the zero-crossing scale, both of which depend on halo mass and f_{NL} . We fit for the parameters $\{m, r_X\}$ over the range of radii

($l_{\text{soft}} < r < r_{\text{vir1}}$), and the resultant model fits are shown in Fig. 7 as the solid lines. The best fit parameters as a function of halo mass are shown in Fig. 8, where we see that, for all but the lowest mass bin in the $f_{\text{NL}} = 100$ model, the values of r_X increase with increasing mass and that these are almost identical for both the positive and negative f_{NL} models. On the other hand, the values for the slope m monotonically decrease (increase) for f_{NL} positive (negative). Modulo the sign, these values are similar for both f_{NL} models.

To use this correction ratio in the halo model, we spline fit $\{r_X, m\}$ as a function of mass, with the exception of the lowest mass bin. We assume that the asymptotic limit for low masses is $R_\rho \rightarrow 1$ as $M \rightarrow 0$ and enforce this by adding $\{r_X, m\} = \{0, 0\}$ for $M = 10^6 h^{-1} M_\odot$ as an extra data point in the spline fitting.

What is actually required for the calculation of the power spectrum is the mass normalized Fourier transforms of the density profiles, and we show this in Fig. 9. We calculate the Fourier transform of the profile as in Eq. (59). Unfortunately, owing to the radial dependent correction factor Eq. (61), there is no analytic solution to this integral and so we compute this numerically. We do however make the following improvement to computational speed: The profile can be rewritten

$$U(k|M, f_{\text{NL}}) = U(k|M)R_\rho[k, M, f_{\text{NL}}], \quad (62)$$

where $U(k|M)$ is given by Eq. (60). We then generate a

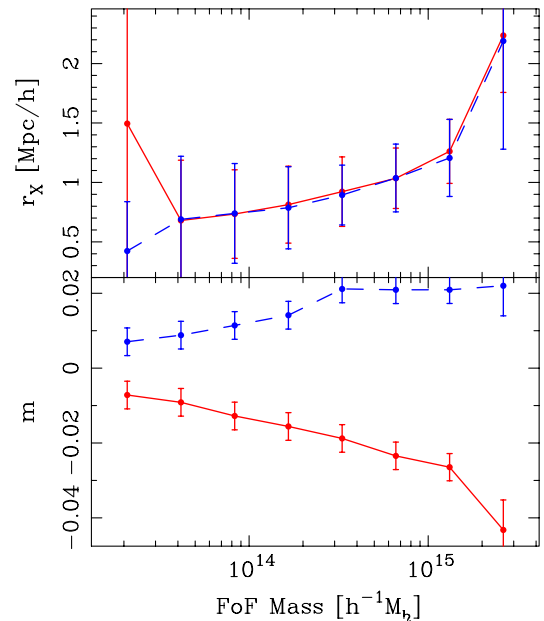


FIG. 8 (color online). Best fit parameters for the density profile ratio $R_\rho(f_{\text{NL}}, M)$, as defined in Eq. (61), as a function of the FoF halo mass, measured at $z = 0$. Top panel: The zero-crossing parameter r_X . Bottom panel: The slope parameter m . The solid red lines denote the results for $f_{\text{NL}} = 100$ and the blue dashed lines the results for $f_{\text{NL}} = -100$.

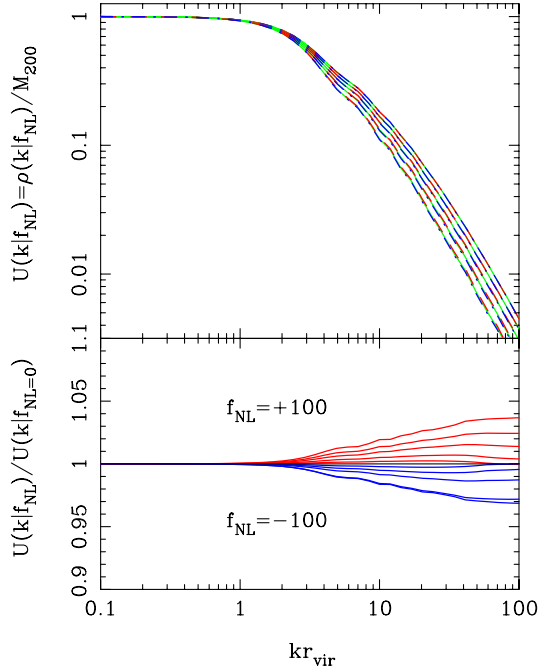


FIG. 9 (color online). Dependence of the Fourier transform of the mass normalized density profile on scale for several halo masses. Top panel: Absolute value of the Fourier transform of the profile [$U(k|M) = \rho(k|M)/M$] as a function of wave number in units of inverse virial radius. The solid green, dashed red, and dot-dashed blue lines show results for $f_{\text{NL}} \in [0, +100, -100]$, respectively. The curves from top to bottom show results for haloes with masses $M \in [5.0 \times 10^{13}, 1.0 \times 10^{14}, 5.0 \times 10^{14}, 1.0 \times 10^{15}, 5.0 \times 10^{15}] h^{-1} M_{\odot}$. Bottom panel: Ratio of the non-Gaussian to Gaussian profiles in Fourier space. The higher mass haloes show stronger amplification (suppression) for $f_{\text{NL}} = 100$ (-100).

bicubic spline (see [75] for details) fit to the ratio $R_{\tilde{\rho}}$ as a function of kr_{vir} and halo mass M . As a final note, the above expression is not normalized correctly in that $U(k|M, f_{\text{NL}})$ does not approach unity on large scales. We are however free to renormalize $U(k|M, f_{\text{NL}})$ and this can be done through the operation $\tilde{U}(k|M, f_{\text{NL}}) = U(k|M, f_{\text{NL}})/U(k=0|M, f_{\text{NL}})$.

VI. RESULTS

We now put together all of the components of the halo model and make predictions for the nonlinear matter power spectrum and the matter correlation function in the Gaussian case and then for the models with local PNG. A practical note on evaluating the 2-halo term for the mass distribution: We are required to compute integrals over an infinite domain in halo mass. This is computationally challenging, and so instead we make the following approximation:

$$P_{2\text{H}} \rightarrow P_{\text{NL}} \left[\frac{1}{\tilde{\rho}} \int_{M_1}^{M_2} dM n(M) M b(M) U(k|M) \right]^2, \quad (63)$$

where $\tilde{\rho} = \int_{M_1}^{M_2} dM n(M) M b(M)$. Provided M_1 and M_2 are sufficiently small and large halo masses, then the above integral approaches the exact answer of infinite limits over a restricted range of k . We set $\{M_1, M_2\} = \{1.0 \times 10^6, 1.0 \times 10^{16}\} h^{-1} M_{\odot}$.

A. Estimating the power spectrum

The density Fourier modes were estimated using the conventional fast Fourier transform method: The dark matter particles were assigned to a regular cubical grid using the ‘‘cloud-in-cell’’ scheme [76], and throughout we used $N_g = 1024^3$ sized Fourier meshes. The fast Fourier transform of the gridded density field was then computed using the FFTW routines [77]. Each resulting Fourier mode was corrected for the convolution with the mesh by dividing out the Fourier transform of the mass-assignment window function. For the cloud-in-cell algorithm this corresponds to the following operation:

$$\delta_d(\mathbf{k}) = \frac{\delta_g(\mathbf{k})}{W(\mathbf{k})}; \quad W(\mathbf{k}) = \prod_{i=1}^3 \left[\frac{\sin[\pi k_i / 2k_{\text{Ny}}]}{[\pi k_i / 2k_{\text{Ny}}]} \right]^2, \quad (64)$$

where subscript d and g denote discrete and grid quantities, respectively, and where $k_{\text{Ny}} = \pi N_g / L$ is the Nyquist frequency.

The discrete power spectra on scale k_l are then estimated by performing the following sums:

$$\hat{P}_d(k_l) = \frac{V_{\mu}}{N_k} \sum_{l=1}^{N_k} |\delta_d(\mathbf{k}_l)|^2, \quad (65)$$

where N_k is the number of Fourier modes in a spherical shell in k space of thickness Δk .

B. Matter power spectrum: Gaussian case

Figure 10 presents the nonlinear matter power spectra measured in the simulations for the Gaussian case at redshifts $z = 1.0$ and $z = 0.0$, left and right panels, respectively. The top sections of the panels show the absolute power and the lower ones the ratio with respect to the predictions from HALOFIT [58]. The figure also shows a term by term breakdown of the halo model predictions. It can clearly be seen that the sum $P_{1\text{H}} + P_{2\text{H}}$ without subtracting the exclusion term overshoots the measured nonlinear power by a factor of 2–3 (green triple-dot-dashed line). The subtraction of the term due to halo exclusion $P_{1\text{H}} + P_{2\text{H}} - P_{2\text{H}}^{\text{Exc}}$ significantly improves the predictions of the model on all scales and at both of the redshifts considered. We see that at $z = 0.0$ the total halo model result is within a few percent of the measured power from the numerical simulations on all scales measured. At $z = 1.0$ the same statement is true except on small scales, $k > 0.5 h \text{Mpc}^{-1}$, where there appears to be a significant disagreement of the order of 20%; this is partly due to the failure of HALOFIT on these scales (which is the input

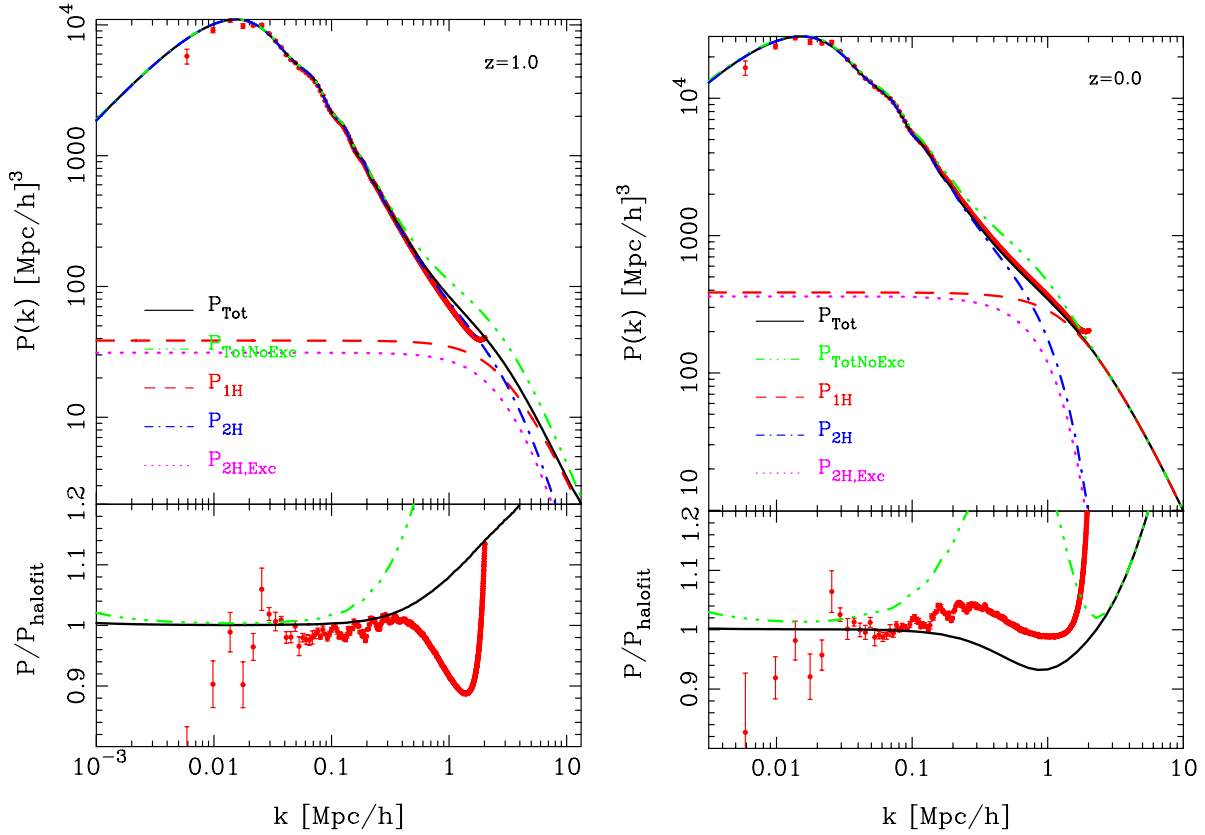


FIG. 10 (color online). Comparison of the matter power spectrum in the halo model and measurements from an ensemble of numerical simulations (see Sec. III for details). Top panel: Absolute power. Points with error bars show estimates from the simulations. The halo model predictions are red dash line denotes P_{1H} ; blue dot-dashed line denotes P_{2H} ; magenta dotted line represents P_{2H}^{Exc} ; the black solid line shows the total halo model prediction including subtraction of the halo exclusion term; the green triple-dot-dashed curve is the same but neglecting the halo exclusion term. Bottom panel: Ratio of the matter power spectra with predictions from HALOFIT [58]. Points and line styles are as above.

nonlinear power spectrum for the 2-halo term). Improving the modeling of the halo-halo center clustering will most likely solve this issue. This discrepancy may also be alleviated by the facts that the Nyquist frequency for the power spectra is $k_{Ny} = \pi 1024/1600 \sim 2.0 h \text{ Mpc}^{-1}$ and that one should only really trust the results up to $k_{Ny}/2 \sim 1.0 h \text{ Mpc}^{-1}$.

On large scales we see that the P_{1H} term (dashed red line) asymptotes to a constant value $\sim \{40, 400\} h^{-3} \text{ Mpc}^3$ at $z = 1$ and $z = 0.0$, respectively. This is significantly larger than the expected amplitude due to the shot noise of the particles $1/\bar{n} = V/N \sim 3.8 h^{-3} \text{ Mpc}^3$. The term P_{2H}^{Exc} (magenta dotted line) effectively kills the excess shot noise of the 1-halo term. This is entirely consistent with the theoretical expectations in Appendix B. The subtraction of the term due to halo exclusion therefore is an essential correction to make in order to obtain realistic predictions in the halo model.

C. Matter power spectrum: PNG case

Figure 11 shows the effects of PNG on the matter power spectrum at redshifts $z = 1$ and $z = 0$, left and right sub-

figures, respectively. The measurements with errors are the ensemble average power obtained from the 12 realizations per f_{NL} . The predictions from the halo model calculation are also plotted and we see good agreement. However, the difference between the $f_{NL} = \{0, +100, -100\}$ models is very small, so we take the ratio of the PNG models with respect to the Gaussian case, and this is what is plotted in the lower sections of the figures. This clearly shows, as was seen earlier in Fig. 2, that the changes are of the order of $\sim 3.5\%$ at $z = 1.0$ and of the order of $\sim 2.5\%$ at $z = 0.0$. The halo model predictions for this ratio are in excellent agreement with the measured ratios.

The strength of the effect appears to peak around $k \sim 1$ and then declines at higher k . This can be understood in the following way: As one goes to higher k the 1-halo term comes to dominate. The integrand for this is $n(M)M^2 U(k|M)$, and for cluster-mass scales it peaks around $k \sim 1$ and then decays strongly, whereas for group- and galaxy-mass scales it peaks at much higher k . As we have seen earlier in Sec. V, the effect of PNG on the mass function and density profiles is strongest for the highest mass haloes. This then leads us to expect that the

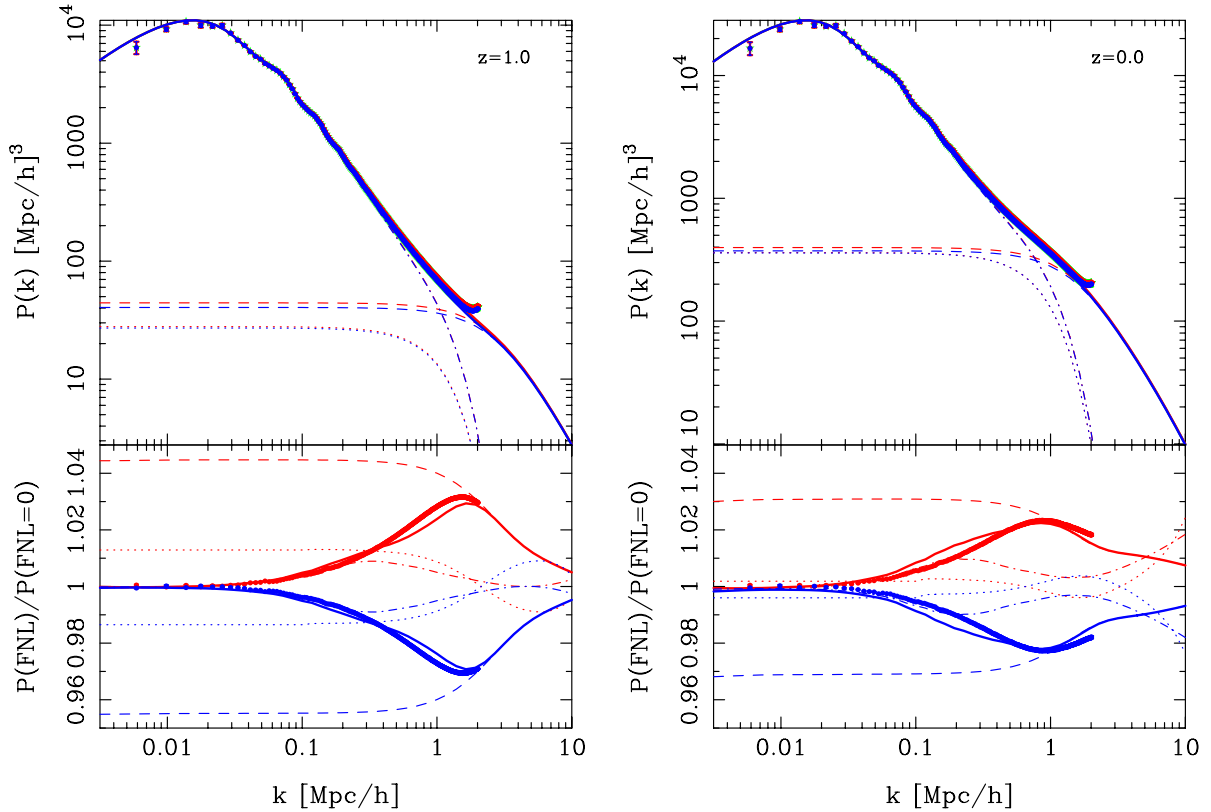


FIG. 11 (color online). Comparison of the matter power spectrum in models with Gaussian and non-Gaussian initial density fluctuations at redshifts $z = 1.0$ (left subfigure) and $z = 0.0$ (right subfigure). Top panels: Absolute power. Points with error bars show results for the simulations and the colors green, red, and blue denote the models $f_{\text{NL}} = \{0, +100, -100\}$, respectively. The lines represent halo model predictions: Dashed lines denote $P_{1\text{H}}$; dot-dashed lines denote $P_{2\text{H}}$; dotted lines denote $P_{2\text{H}}^{\text{Exc}}$; the solid line represents the total halo model prediction including subtraction of the halo exclusion term. Bottom panels: Ratio of the matter power spectra in the $f_{\text{NL}} = +100$ and -100 models with respect to the Gaussian ($f_{\text{NL}} = 0$) results. Points and line styles are as above.

effect of PNG on the nonlinear power spectrum should peak around $k \sim 1$. The dashed lines in Fig. 11 show the 1-halo term and so give confirmation of this logic.

D. Matter correlation function: Gaussian case

We estimate the matter correlation function for the $z = 1$ and $z = 0$ snapshots in each simulation to an accuracy of the order of 3%–5% using our fast and exact correlation code DUALTREETWOPOINT, which is based upon the k D-tree data structure, and the code is parallelized using message passing interface calls. Thus on averaging over the 12 simulations we expect results that are accurate to $5\%/\sqrt{12-1} \approx 2\%$.

Figure 12 presents the ensemble average estimate of the matter correlation function in the Gaussian models over three decades in spatial scale at redshifts $z = 1.0$ and $z = 0.0$, left and right panels, respectively. The figure also shows the halo model predictions appear in remarkably good agreement with the simulation data. The exact deviations are hard to quantify on the log scale and so we take the ratio of the theory and simulation measurements with respect to the HALOFIT model correlation function.

We now see that the halo model predictions are better than 10% over the entire range of scales and redshifts considered. The predictions are somewhat worse at the 2- to 1-halo crossover scale (i.e. $r \in [2, 10] h^{-1} \text{Mpc}$) and also on the very largest of scales around the BAO feature and on the smallest scales $r \leq 0.2 h^{-1} \text{Mpc}$. We emphasize that none of the halo model parameters were tuned to fit the clustering statistics directly.

In the figure we also show the result for the halo model calculation if no exclusion correction is made, and we see that predictions significantly overshoot the measurements by factors of a few on small scales, especially at low redshift. The figure also shows that the exclusion correction essentially kills the contribution from the 2-halo term to the correlation function on small scales. Furthermore this correction also kills some of the contribution of the 1-halo term to the correlation function on scales larger than $r \sim 2 h^{-1} \text{Mpc}$.

E. Matter correlation function: PNG case

In Fig. 13 we present the ensemble average estimate of the matter correlation function in the models evolving from

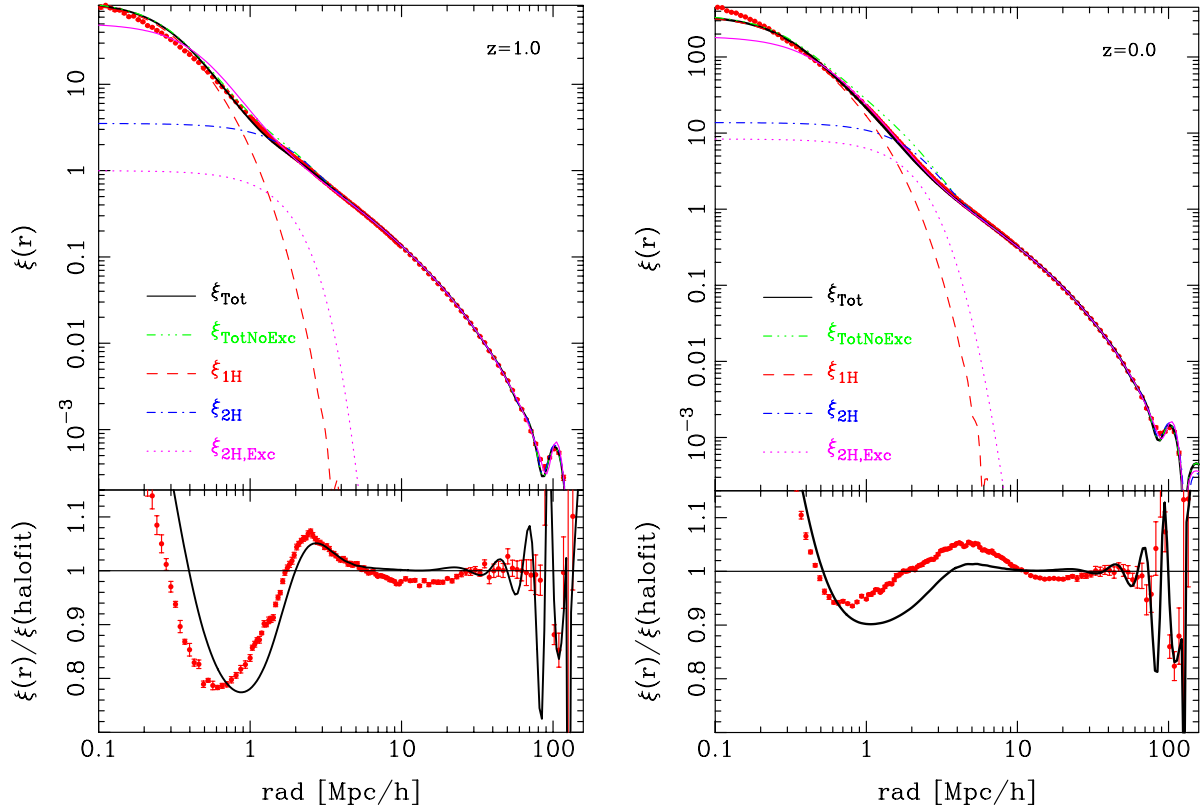


FIG. 12 (color online). Matter correlation function as a function of spatial scale measured in the Gaussian simulations at redshifts $z = 1.0$ (left subfigure) and $z = 0.0$ (right subfigure). Top panels: Absolute correlation function. Points with errors denote the measurements from the simulations and the lines denote the halo model predictions: Dashed lines denote ξ_{1H} ; dot-dashed lines denote ξ_{2H} ; dotted lines denote $\xi_{2H,Exc}^{Exc}$; solid lines represent the total halo model prediction including subtraction of the halo exclusion term; triple dot-dashed lines show the same but without subtracting the exclusion term. Bottom panel: Ratio of the measurements and halo model predictions with respect to the nonlinear correlation function from HALOFIT.

PNG initial conditions at redshifts $z = 1.0$ and $z = 0.0$, left and right panels, respectively. As for the correlation function in the Gaussian case the halo model predictions with exclusion provide a remarkably good description of the clustering. The differences are not clearly visible on the log scale, and so we take the ratio of the PNG models with the Gaussian case. Note that we construct this ratio for each simulation and compute the ensemble average.

The lower panels of the figures show that, as in the case for the matter power spectrum, there is a significant signal of f_{NL} on the small-scale correlation function. At $z = 0.0$ the signal is of the order of $\sim 2.5\%$ and affects the clustering on scales $r < 5 h^{-1} \text{Mpc}$. At higher redshift $z = 1$, we clearly see the same general trend but the relative difference in the signal is a little larger $\sim 3\% - 4\%$. However, the measurements appear slightly noisier.

Once again the halo model predictions with exclusion provide an excellent description of the ratio, being accurate to $\sim 1\%$ precision.

VII. CONCLUSIONS

In this paper we have developed the halo model of large-scale structure for application to computing matter

clustering statistics in models with PNG initial conditions. In particular, we considered the case of local quadratic corrections to the primordial potential, characterized by the parameter f_{NL} ; see Sec. II for details.

In Sec. III we provided details of the large ensemble of N -body simulations that we employed in this study.

In Sec. IV we explored standard nonlinear perturbation theory techniques to predict the matter power spectrum in models with PNG. It was demonstrated that the next-to-leading-order correction to the power spectrum worked very well up to scales $k < 0.2 h \text{Mpc}^{-1}$ for the ratio with respect to the Gaussian case, but that on smaller scales the PT failed to reproduce the simulation results. Further, the absolute power was only well reproduced by the PT on scales $< 0.1 h \text{Mpc}^{-1}$.

In Sec. IV, we reviewed the halo model and gave a calculation of halo exclusion. In Appendix B we also showed theoretically that exclusion can help resolve the problem of the large-scale excess power in the halo model.

In Sec. V we performed a numerical study of the ingredients of the halo model, in the context of PNG. We studied the halo mass function, the halo bias, and the density profiles. For the mass function ratios, we confirmed that

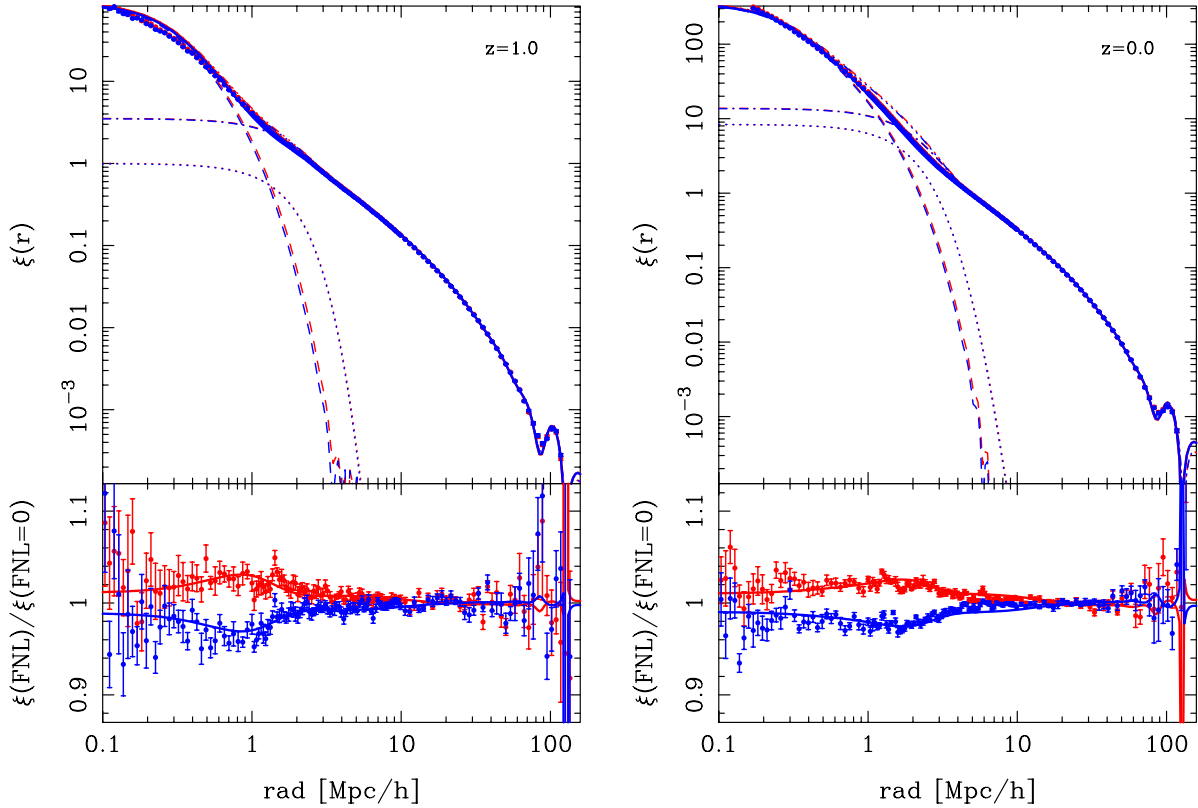


FIG. 13 (color online). Comparison of the matter correlation function in models with Gaussian and non-Gaussian initial density fluctuations at redshifts $z = 1.0$ (left subfigure) and $z = 0.0$ (right subfigure). Top panels: Absolute correlation function. Points with errors show results for the simulations and the colors green, red, and blue denote the models $f_{\text{NL}} = \{0, +100, -100\}$, respectively. The lines represent halo model predictions: Dashed lines denote $\xi_{1\text{H}}$; dot-dashed lines denote $\xi_{2\text{H}}$; dotted lines denote $\xi_{2\text{H}}^{\text{Exc}}$; the solid line represents the total halo model prediction including subtraction of the halo exclusion term. Bottom panels: Ratio of the matter correlation functions with $f_{\text{NL}} = +100$ and -100 with respect to the Gaussian ($f_{\text{NL}} = 0$) results. Points and line styles are as above.

the existing models of LV [68] and MVJ [13] were in excellent agreement with the simulations, once the peak height was rescaled [20]. We found that the Gaussian mass function of Sheth and Tormen [62] was a poor description of the simulation data.

In Sec. V we examined the halo bias in the context of PNG and showed that, if the halo model is correct, then there must be a small asymmetry in the scale dependence of the bias in non-Gaussian models on large scales.

In Sec. V we explored the density profiles of dark matter haloes in the context of PNG. This has not been undertaken before and we showed that halo profiles become more (less) dense in the presence of $f_{\text{NL}} > 0$ ($f_{\text{NL}} < 0$). We found, for $f_{\text{NL}} = \pm 100$, that cluster-, group-, and small-group-mass haloes were modified at the level of $\{\lesssim \pm 4.5\%, \pm \lesssim \pm 3.5\%, \lesssim \pm 2.5\%\}$. We modeled these effects with a simple log-linear model.

In Sec. VI we presented the two-point clustering statistics of the matter in the simulations and in the halo model. We showed that including halo exclusion in the model was important in order to produce accurate results. We also demonstrated that on large scales the halo exclusion term almost exactly canceled the excess large-scale power arising

in the 1-halo term. This appears to solve a long-standing technical problem for the halo model.

For the case of the absolute power spectra, while the theory and the measurements differed by up to 10%, the ratio of the non-Gaussian to Gaussian predictions and measurements differed by of the order of $\sim 1\%$. For the case of the correlation functions, the absolute predictions on small scales were very good and the ratio of the non-Gaussian to Gaussian predictions and measurements were also accurate to $\sim 1\%$.

We conclude that the modeling that we have developed in this paper will be good enough for predicting the absolute value of matter clustering statistics to within $\lesssim 10\%$ and their ratios to $\lesssim 1\%$. We anticipate that this will be useful for constraining f_{NL} from measurements of the nonlinear shear correlation function in future weak lensing surveys such as EUCLID [32] and LSST [33].

ACKNOWLEDGMENTS

We thank Adam Amara, Tsz Yan Lam, Cristiano Porciani, Roman Scoccimarro, Emiliano Sefusatti, Ravi Sheth, and Uros Seljak for useful discussions. We kindly

thank V. Springel for making public GADGET-2 and for providing his B-FOF halo finder. R. E. S. and V. D. acknowledge the hospitality of the ‘‘Centro de Ciencias de Bensque–Pedro Pascual’’ where some of this work was performed. R. E. S. acknowledges support from a Marie Curie Reintegration Grant and the Alexander von Humboldt foundation. R. E. S. and V. D. were partly supported by the Swiss National Foundation under Contract No. 200021-116696/1 and WCU Grant No. R32-2008-000-10130-0. V. D. was also partly supported by the University of Zurich under Contract FK UZH 57184001. L. M. was supported by the Deutsche Forschungsgemeinschaft under Grant No. DFG-MA 4967/1-1.

APPENDIX A: SOME RESULTS CONCERNING THE PRIMORDIAL SKEWNESS

In this appendix we give some relations concerning the skewness of the density field. The ensemble average of the cube of the density field using Fourier space representation can be written

$$\langle \delta_M^3(x) \rangle = \int \frac{d^3 \mathbf{k}_1}{(2\pi)^3} \frac{d^3 \mathbf{k}_2}{(2\pi)^3} \frac{d^3 \mathbf{k}_3}{(2\pi)^3} W(k_1, M) W(k_2, M) W(k_3, M) \times \langle \delta(\mathbf{k}_1) \delta(\mathbf{k}_2) \delta(\mathbf{k}_3) \rangle e^{-i(\mathbf{k}_1 + \mathbf{k}_2 + \mathbf{k}_3) \cdot \mathbf{x}}. \quad (\text{A1})$$

For a Gaussian field the average of the three Fourier modes gives zero, but for the local model of non-Gaussianity the product is related to the primordial potential bispectrum. Using Eqs. (4), (5), and (9), we arrive at

$$\begin{aligned} \langle \delta_M^3(x) \rangle &= \int \frac{d^3 \mathbf{k}_1}{(2\pi)^3} \frac{d^3 \mathbf{k}_2}{(2\pi)^3} \frac{d^3 \mathbf{k}_3}{(2\pi)^3} W(k_1, M) W(k_2, M) W(k_3, M) \alpha(k_1) \alpha(k_2) \alpha(k_3) \langle \Phi(\mathbf{k}_1) \Phi(\mathbf{k}_2) \Phi(\mathbf{k}_3) \rangle \exp[-i(\mathbf{k}_1 + \mathbf{k}_2 + \mathbf{k}_3) \cdot \mathbf{x}] \\ &= \int \frac{d^3 \mathbf{k}_1}{(2\pi)^3} \frac{d^3 \mathbf{k}_2}{(2\pi)^3} \frac{d^3 \mathbf{k}_3}{(2\pi)^3} W(k_1, M) W(k_2, M) W(k_3, M) \alpha(k_1) \alpha(k_2) \alpha(k_3) B_\Phi(\mathbf{k}_1, \mathbf{k}_2, \mathbf{k}_3) (2\pi)^3 \delta(\mathbf{k}_1 + \mathbf{k}_2 + \mathbf{k}_3) \\ &\quad \times \exp[-i(\mathbf{k}_1 + \mathbf{k}_2 + \mathbf{k}_3) \cdot \mathbf{x}] \\ &= \int \frac{d^3 \mathbf{k}_1}{(2\pi)^3} \frac{d^3 \mathbf{k}_2}{(2\pi)^3} \frac{d^3 \mathbf{k}_3}{(2\pi)^3} W(k_1, M) W(k_2, M) W(k_3, M) \alpha(k_1) \alpha(k_2) \alpha(k_3) 2f_{\text{NL}} [P_\phi(k_1) P_\phi(k_2) \\ &\quad + 2\text{cyc}] (2\pi)^3 \delta(\mathbf{k}_1 + \mathbf{k}_2 + \mathbf{k}_3) \exp[-i(\mathbf{k}_1 + \mathbf{k}_2 + \mathbf{k}_3) \cdot \mathbf{x}]. \end{aligned} \quad (\text{A2})$$

Computing the delta function integrals separately for each of the three terms in square brackets and defining $k_3^2 \equiv k_1^2 + k_2^2 + 2k_1 k_2 \mu$, we then find that the skewness ($S_3 \equiv \langle \delta^3 \rangle / \langle \delta^2 \rangle^2$) has the form

$$\begin{aligned} S_3 \sigma^4 &= 3f_{\text{NL}} \int \frac{d^3 \mathbf{k}_1}{(2\pi)^3} \frac{d^3 \mathbf{k}_2}{(2\pi)^3} \alpha(k_1) P_\phi(k_1) \alpha(k_2) P_\phi(k_2) \\ &\quad \times \int_{-1}^1 d\mu \alpha(k_3) [W(k_1, M) W(k_2, M) W(k_3, M)]. \end{aligned} \quad (\text{A3})$$

We are also interested in computing the derivatives of the skewness with respect to the mass variance σ up to second order:

$$\frac{d(S_3 \sigma^4)}{d \log \sigma} = \frac{1}{3} \frac{d \log M}{d \log \sigma} \frac{d(S_3 \sigma^4)}{d \log R}; \quad (\text{A4})$$

$$\frac{d^2(S_3 \sigma^4)}{(d \log \sigma)^2} = \frac{1}{3} \frac{d^2 \log M}{(d \log \sigma)^2} \frac{d(S_3 \sigma^4)}{d \log R} + \frac{1}{9} \left(\frac{d \log M}{d \log \sigma} \right)^2 \frac{d^2(S_3 \sigma^4)}{d \log R^2}, \quad (\text{A5})$$

where we used the fact that $d \log M / d \log R = 3$. The required auxiliary functions are

$$\begin{aligned} \frac{d(S_3 \sigma^4)}{d \log R} &= 3f_{\text{NL}} \int \frac{d^3 \mathbf{k}_1}{(2\pi)^3} \frac{d^3 \mathbf{k}_2}{(2\pi)^3} \alpha(k_1) P_\phi(k_1) \alpha(k_2) P_\phi(k_2) \\ &\quad \times \int_{-1}^1 d\mu \alpha(k_3) [W'_1 W_2 W_3 + W_1 W'_2 W_3 + W_1 W_2 W'_3]; \end{aligned} \quad (\text{A6})$$

$$\begin{aligned} \frac{d^2(S_3 \sigma^4)}{d \log R^2} &= 3f_{\text{NL}} \int \frac{d^3 \mathbf{k}_1}{(2\pi)^3} \frac{d^3 \mathbf{k}_2}{(2\pi)^3} \alpha(k_1) P_\phi(k_1) \alpha(k_2) P_\phi(k_2) \\ &\quad \times \int_{-1}^1 d\mu \alpha(k_3) [W''_1 W_2 W_3 + W_1 W''_2 W_3 \\ &\quad + W_1 W_2 W''_3 + 2W'_1 W'_2 W_3 + 2W'_1 W_2 W'_3 \\ &\quad + 2W_1 W'_2 W'_3]; \end{aligned} \quad (\text{A7})$$

$$\frac{d \log \sigma^2(R)}{d \log M} = \frac{2}{3\sigma^2(R)} \int \frac{d^3 \mathbf{k}_1}{(2\pi)^3} P_{\text{Lin}}(k_1) W_1 W'_1; \quad (\text{A8})$$

$$\begin{aligned} \frac{d^2 \log \sigma^2(R)}{d \log M^2} &= \frac{2}{9\sigma^2(R)} \int \frac{d^3 \mathbf{k}_1}{(2\pi)^3} P_{\text{Lin}}(k_1) [W_1^2 + W_1 W''_1] \\ &\quad - \left[\frac{d \log \sigma^2(R)}{d \log M} \right]^2, \end{aligned} \quad (\text{A9})$$

where we have introduced the notation $W_i \equiv W(k_i R)$, $W'_i \equiv dW(k_i R)/d\log(k_i R)$, and $W''_i \equiv d^2W(k_i R)/d\log(k_i R)^2$. For a real-space top hat filter function we have

$$W_{\text{TH}}(y) = \frac{3}{y^3}[\text{siny} - y \text{cosy}]; \quad (\text{A10})$$

$$W'_{\text{TH}}(y) = \frac{3}{y^3}[(y^2 - 3) \text{siny} + 3y \text{cosy}]; \quad (\text{A11})$$

$$W''_{\text{TH}}(y) = \frac{3}{y^3}[(9 - 4y^2) \text{siny} + y(y^2 - 9) \text{cosy}]. \quad (\text{A12})$$

Finally, some relationships that will be of use for calculating the halo mass function and also the scale-independent contribution to the halo bias are

$$\frac{d\log(\sigma S_3)}{d\log\nu} = \frac{1}{\sigma^3} \left[\sigma^4 S_3 - \frac{d(\sigma^4 S_3)}{d\log\sigma} \right]; \quad (\text{A13})$$

$$\frac{d^2\log(\sigma S_3)}{d\log\nu^2} = \frac{1}{\sigma^3} \left[3\sigma^4 S_3 - 4 \frac{d(\sigma^4 S_3)}{d\log\sigma} + \frac{d^2(\sigma^4 S_3)}{d\log\sigma} \right]. \quad (\text{A14})$$

APPENDIX B: A POSSIBLE SOLUTION TO THE PROBLEM OF EXCESS POWER ON LARGE SCALES IN THE HALO MODEL

Several authors have pointed out that the halo model fails to reproduce the correct clustering statistics on large scales [51,58,61,78]. This arises because the 1-halo term approaches a constant value significantly in excess of the shot noise for dark matter particles in simulations, e.g.

$$\lim_{k \rightarrow 0} P_{\text{1H}}(k) = \frac{1}{\bar{\rho}^2} \int_0^\infty dM n(M) M^2 \gg \frac{1}{\bar{n}_\delta}, \quad (\text{B1})$$

where \bar{n}_δ is the number density of dark matter particles. A more recent criticism of the halo model, in the context of RPT, was given by [61]. We now show how halo exclusion may resolve this issue.

Consider the RPT formulation of the nonlinear matter power spectrum in the perturbation theory [61]:

$$P_{\text{RPT}}(k) = G^2(k)P_{\text{Lin}}(k) + P_{\text{MC}}(k), \quad (\text{B2})$$

where $G(k)$ is the nonlinear density propagator, which informs us of how a density mode decorrelates from its initial state; and the term P_{MC} informs us of the power gained by a single mode from coupling with all other modes. The authors of [61] make the analogy $P_{\text{2H}} \rightarrow G^2(k)P_{\text{Lin}}$ and $P_{\text{1H}} \rightarrow P_{\text{MC}}(k)$. They then measure the quantity $P - G^2(k)P_{\text{Lin}}$ from simulations and compare the result with the theoretical predictions for $P_{\text{MC}} \propto k^4$ and $P_{\text{1H}} \propto \text{const}$. The simulations show a k^4 slope, and

hence they conclude that the halo model fails on large scales.

Let us now reexamine this issue in the context of halo exclusion. First, consider again the halo-center clustering of haloes of masses M_1 and M_2 ; if we treat this as in [53] and expand the halo density as a local function of the nonlinear dark matter density, then we have

$$P_{\text{cent}}^{\text{hh}} = b_1(M_1)b_1(M_2)P_{\text{NL}}(k|R) + \mathcal{O}(b_2, b_3, \dots). \quad (\text{B3})$$

Consider now the very large-scale limit of the halo model, and then we have $U \rightarrow 1$ as $k \rightarrow 0$. Recalling the conditions Eqs. (48), (49), and (52), the halo model then reduces to

$$P_{\text{HM}}(k) = P_{\text{NL}}(k|R) - P_{\text{2H}}^{\text{exc}}(\mathbf{k}) + P_{\text{1H}}(k). \quad (\text{B4})$$

If we now insert the RPT expansion for the large-scale smoothed nonlinear matter power spectrum, then we have

$$P_{\text{HM}}(k) = |W(k|R)|^2 [G^2(k)P_{\text{Lin}}(k) + P_{\text{MC}}(k)] - P_{\text{2H}}^{\text{exc}}(\mathbf{k}) + P_{\text{1H}}(k). \quad (\text{B5})$$

On rearranging the above equation, one finds

$$P_{\text{HM}}(k) - |W(k|R)|^2 G^2(k)P_{\text{Lin}}(k) = |W(k|R)|^2 P_{\text{MC}}(k) - P_{\text{2H}}^{\text{exc}}(\mathbf{k}) + P_{\text{1H}}(k). \quad (\text{B6})$$

In the limit $k \rightarrow 0$, $W(k|R) \rightarrow 1$. The right-hand side of the above equation can be consistent with the simulation results of [61], if and only if $P_{\text{1H}} - P_{\text{2H}}^{\text{exc}} \rightarrow \epsilon$, where ϵ is a sufficiently small quantity that the right side of the above equation decays as $\propto k^4$ for all observable scales of interest. Using Eq. (34) we may explicitly write ϵ as

$$\epsilon \equiv \frac{1}{\bar{\rho}^2} \int dM n(M) M^2 - \prod_{i=1}^2 \left\{ \frac{1}{\bar{\rho}} \int dM_i n(M_i) M_i \right\} V(r_1 + r_2) \times [1 + b(M_1)b(M_2)\bar{\xi}_{\text{NL}}(r_1 + r_2)]. \quad (\text{B7})$$

On taking the relation between halo volume and mass to be $M_{\text{vir}} = 4\pi r_{\text{vir}}^3 \Delta \bar{\rho} / 3$, where Δ is an overdensity threshold that defines the halo today, e.g. $\Delta \sim 200$, then we may expand the exclusion volume in powers of the halo mass:

$$V(r_1 + r_2) = \frac{1}{\bar{\rho} \Delta} [M_1 + 3M_1^{2/3}M_2^{1/3} + 3M_1^{1/3}M_2^{2/3} + M_2]. \quad (\text{B8})$$

On inserting this into the second term on the left side of Eq. (B7) we find

$$\begin{aligned} &\rightarrow \frac{1}{\bar{\rho}^3 \Delta} \int dM_1 n(M_1) M_1 \int dM_2 n(M_2) M_2 \\ &\quad \times [2M_1 + 6M_1^{2/3} M_2^{1/3}] [1 + b(M_1) b(M_2) \bar{\xi}_{\text{NL}}(r_1 + r_2)]. \end{aligned} \quad (\text{B9})$$

Let us consider two possible limits of the above expression:

(i) $\bar{\xi}_{\text{NL}} \ll 1$: Then we have

$$\begin{aligned} &\rightarrow \frac{1}{\bar{\rho}^3 \Delta} \int dM_1 n(M_1) M_1 \\ &\quad \times \int dM_2 n(M_2) M_2 [2M_1 + 6M_1^{2/3} M_2^{1/3}] \\ &= \frac{2}{\bar{\rho}^2 \Delta} \int dM_1 n(M_1) M_1^2 \\ &\quad + \frac{6}{\bar{\rho}^3 \Delta} \int dM_1 n(M_1) M_1^{5/3} \int dM_2 n(M_2) M_2^{4/3}. \end{aligned} \quad (\text{B10})$$

(ii) $\bar{\xi}_{\text{NL}} \gg 1$: Then we have

$$\begin{aligned} &\rightarrow \frac{1}{\bar{\rho}^3 \Delta} \int dM_1 n(M_1) M_1 b(M_1) \int dM_2 n(M_2) M_2 b(M_2) \\ &\quad \times [2M_1 + 6M_1^{2/3} M_2^{1/3}] \bar{\xi}_{\text{NL}}(r_1 + r_2). \end{aligned} \quad (\text{B11})$$

To get an estimate of this, suppose that the first term in Eq. (B11) dominates over the second and that

$\max[\bar{\xi}_{\text{NL}}(r_1 + r_2 | R)] \sim f \Delta$, and then we would have

$$\rightarrow \epsilon \approx \frac{1}{\bar{\rho}^2} \int dM n(M) M^2 [1 - 2fb(M)]. \quad (\text{B12})$$

We thus see that the correction can be very close to the order of the resulting large-scale power for the 1-halo term and depends strictly on the quantity $1 - 2fb(M)$. We note that the case $f = 1$ would mean $\bar{\xi} \sim \Delta$ and that this would be unrealistically large. This may be argued in the following way: Δ is the volume average density at the viral radius, whereas $b_1(M_1) b_1(M_2) \bar{\xi}_{\text{NL}}(r_1 + r_2 | r)$ is the volume average correlation function of halo centers smoothed on the scale R , for separations $r_1 + r_2$, and excluding the points within the same halo; thus we conclude that $f < 1$. In fact we would need $\max[\bar{\xi}_{\text{NL}}(r_1 + r_2 | R)] < \Delta / 2b(M)$.

As we show in Fig. 10, exact evaluation of the 1-halo and the 2-halo exclusion terms on large scales produces two quantities that almost exactly cancel. We therefore forward halo exclusion as a risible solution to the problem of excess large-scale power in the halo model.

As this paper was being submitted to the ARXIV, a paper discussing an alternative solution to resolving the breakdown of the halo model on large scales was proposed by [79].

-
- [1] M. Colless *et al.*, [arXiv:astro-ph/0306581](#).
 [2] K.N. Abazajian *et al.*, *Astrophys. J. Suppl. Ser.* **182**, 543 (2009).
 [3] N. Jarosik *et al.*, [arXiv:1001.4744](#).
 [4] E. Komatsu *et al.*, *Astrophys. J. Suppl. Ser.* **192**, 18 (2011).
 [5] C.L. Reichardt *et al.*, *Astrophys. J.* **694**, 1200 (2009).
 [6] M.L. Brown *et al.*, *Astrophys. J.* **705**, 978 (2009).
 [7] The Planck Collaboration, [arXiv:astro-ph/0604069](#).
 [8] A.P.S. Yadav and B.D. Wandelt, *Phys. Rev. Lett.* **100**, 181301 (2008).
 [9] P. Creminelli and M. Zaldarriaga, *J. Cosmol. Astropart. Phys.* **10** (2004) 006.
 [10] B. Grinstein and M.B. Wise, *Astrophys. J.* **310**, 19 (1986).
 [11] J.N. Fry and R.J. Scherrer, *Astrophys. J.* **429**, 36 (1994).
 [12] F. Lucchin and S. Matarrese, *Astrophys. J.* **330**, 535 (1988).
 [13] S. Matarrese, L. Verde, and R. Jimenez, *Astrophys. J.* **541**, 10 (2000).
 [14] R. Scoccimarro, E. Sefusatti, and M. Zaldarriaga, *Phys. Rev. D* **69**, 103513 (2004).
 [15] E. Sefusatti and E. Komatsu, *Phys. Rev. D* **76**, 083004 (2007).
 [16] T. Nishimichi, A. Taruya, K. Koyama, and C. Sabiu, *J. Cosmol. Astropart. Phys.* **07** (2010) 002.
 [17] E. Sefusatti, M. Crocce, and V. Desjacques, *Mon. Not. R. Astron. Soc.* **406**, 1014 (2010).
 [18] N. Dalal, O. Doré, D. Huterer, and A. Shirokov, *Phys. Rev. D* **77**, 123514 (2008).
 [19] V. Desjacques, U. Seljak, and I.T. Iliev, *Mon. Not. R. Astron. Soc.* **396**, 85 (2009).
 [20] M. Grossi, L. Verde, C. Carbone, K. Dolag, E. Branchini, F. Iannuzzi, S. Matarrese, and L. Moscardini, *Mon. Not. R. Astron. Soc.* **398**, 321 (2009).
 [21] A. Pillepich, C. Porciani, and O. Hahn, *Mon. Not. R. Astron. Soc.* **402**, 191 (2010).
 [22] A. Slosar, C. Hirata, U. Seljak, S. Ho, and N. Padmanabhan, *J. Cosmol. Astropart. Phys.* **08** (2008) 031.
 [23] S. Matarrese and L. Verde, *Astrophys. J. Lett.* **677**, L77 (2008).
 [24] A. Taruya, K. Koyama, and T. Matsubara, *Phys. Rev. D* **78**, 123534 (2008).
 [25] E. Sefusatti, *Phys. Rev. D* **80**, 123002 (2009).
 [26] T. Giannantonio and C. Porciani, *Phys. Rev. D* **81**, 063530 (2010).
 [27] V. Desjacques and U. Seljak, *Classical Quantum Gravity* **27**, 124011 (2010).
 [28] J. Xia, A. Bonaldi, C. Baccigalupi, G. De Zotti, S. Matarrese, L. Verde, and M. Viel, *J. Cosmol. Astropart. Phys.* **08** (2010) 013.

- [29] F. De Bernardis, P. Serra, A. Cooray, and A. Melchiorri, *Phys. Rev. D* **82**, 083511 (2010).
- [30] M. Grossi, E. Branchini, K. Dolag, S. Matarrese, and L. Moscardini, *Mon. Not. R. Astron. Soc.* **390**, 438 (2008).
- [31] C. Fedeli and L. Moscardini, *Mon. Not. R. Astron. Soc.* **405**, 681 (2010).
- [32] A. Refregier, A. Amara, T.D. Kitching, A. Rassat, R. Scaramella, J. Weller (f. t. Euclid Imaging Consortium), [arXiv:1001.0061](https://arxiv.org/abs/1001.0061).
- [33] P.A. Abell *et al.* (LSST Science Collaboration), [arXiv:0912.0201](https://arxiv.org/abs/0912.0201).
- [34] D. Huterer and M. Takada, *Astropart. Phys.* **23**, 369 (2005).
- [35] D. Huterer, M. Takada, G. Bernstein, and B. Jain, *Mon. Not. R. Astron. Soc.* **366**, 101 (2006).
- [36] A. Amara and A. Refregier, *Mon. Not. R. Astron. Soc.* **351**, 375 (2004).
- [37] At first glance the nonlinear (in f_{NL}) corrections to the power and bispectrum in Eqs. (3) and (5) appear to be infrared divergent quantities. This can be seen most simply by taking the limit $k \rightarrow 0$, and for the power spectrum this leads to an integral of the form $\int_0^\infty dq q^2 P_\phi^2(q)$. Taking $P_\phi(q) \propto k^{n-4}$, then the above integral becomes $\int_0^\infty dq q^{2(n-4)+2} \propto k^\alpha|_0^\infty$, where $\alpha = 2(n-4) + 3$. Taking $n = 1$, then we get $\alpha = -3$, and we now see that if we substitute the lower limit, then the expression diverges. However, as was pointed out by [26], if one believes that inflation was responsible for the non-Gaussianity, then one should invoke the cutoff scales which limit the physical processes: On small scales the fluctuations are cut off by the reheating scale during inflation, and on the large scales, by the horizon size today. In this case and for realistic values of f_{NL} , then the higher order corrections should be subdominant at the present time and so can be neglected [13,26].
- [38] A. Lewis, A. Challinor, and A. Lasenby, *Astrophys. J.* **538**, 473 (2000).
- [39] V. Springel, *Mon. Not. R. Astron. Soc.* **364**, 1105 (2005).
- [40] Y.B. Zel'Dovich, *Astron. Astrophys.* **5**, 84 (1970).
- [41] M. Davis, G. Efstathiou, C. S. Frenk, and S. D. M. White, *Astrophys. J.* **292**, 371 (1985).
- [42] Note that we assume that haloes, which are found with FoF halo finders in numerical simulations, have a mass M_{FoF} and that this corresponds to $M_{\text{FoF}} \equiv M_{200} = 4/3\pi r_{200}^3 200\bar{\rho}$; i.e. the mean overdensity inside a sphere of radius r_{200} is 200 times the mean background density. The only issue that one must be careful of when dealing with halo phenomenology is that the same mass convention is adopted for all semianalytic models: mass function, profiles, and bias, etc. Where there are clashes of definition, we are careful to obtain mappings between these schemes to ensure consistency following the method of Smith and Watts [43].
- [43] R.E. Smith and P.I.R. Watts, *Mon. Not. R. Astron. Soc.* **360**, 203 (2005).
- [44] F. Bernardeau, S. Colombi, E. Gaztañaga, and R. Scoccimarro, *Phys. Rep.* **367**, 1 (2002).
- [45] M. Crocce and R. Scoccimarro, *Phys. Rev. D* **73**, 063519 (2006).
- [46] N. Bartolo, J.P. Beltrán Almeida, S. Matarrese, M. Pietroni, and A. Riotto, *J. Cosmol. Astropart. Phys.* **03** (2010) 011.
- [47] F. Bernardeau, M. Crocce, and E. Sefusatti, *Phys. Rev. D* **82**, 083507 (2010).
- [48] U. Seljak, *Mon. Not. R. Astron. Soc.* **318**, 203 (2000).
- [49] J. A. Peacock and R. E. Smith, *Mon. Not. R. Astron. Soc.* **318**, 1144 (2000).
- [50] C. Ma and J. N. Fry, *Astrophys. J.* **543**, 503 (2000).
- [51] A. Cooray and R. Sheth, *Phys. Rep.* **372**, 1 (2002).
- [52] R.J. Scherrer and E. Bertschinger, *Astrophys. J.* **381**, 349 (1991).
- [53] R.E. Smith, R. Scoccimarro, and R.K. Sheth, *Phys. Rev. D* **75**, 063512 (2007).
- [54] J. N. Fry and E. Gaztanaga, *Astrophys. J.* **413**, 447 (1993).
- [55] P. Coles, *Mon. Not. R. Astron. Soc.* **262**, 1065 (1993).
- [56] H.J. Mo and S.D.M. White, *Mon. Not. R. Astron. Soc.* **282**, 347 (1996).
- [57] P. McDonald, *Phys. Rev. D* **78**, 123519 (2008).
- [58] R.E. Smith, J.A. Peacock, A. Jenkins, S.D.M. White, C. S. Frenk, F.R. Pearce, P.A. Thomas, G. Efstathiou, and H.M.P. Couchman, *Mon. Not. R. Astron. Soc.* **341**, 1311 (2003).
- [59] M. Takada and B. Jain, *Mon. Not. R. Astron. Soc.* **340**, 580 (2003).
- [60] J.L. Tinker, D.H. Weinberg, Z. Zheng, and I. Zehavi, *Astrophys. J.* **631**, 41 (2005).
- [61] M. Crocce and R. Scoccimarro, *Phys. Rev. D* **77**, 023533 (2008).
- [62] R.K. Sheth and G. Tormen, *Mon. Not. R. Astron. Soc.* **308**, 119 (1999).
- [63] W.H. Press and P. Schechter, *Astrophys. J.* **187**, 425 (1974).
- [64] J.R. Bond, S. Cole, G. Efstathiou, and N. Kaiser, *Astrophys. J.* **379**, 440 (1991).
- [65] M. S. Warren, K. Abazajian, D.E. Holz, and L. Teodoro, *Astrophys. J.* **646**, 881 (2006).
- [66] M. Crocce, P. Fosalba, F.J. Castander, and E. Gaztañaga, *Mon. Not. R. Astron. Soc.* **403**, 1353 (2010).
- [67] M. Manera, R.K. Sheth, and R. Scoccimarro, *Mon. Not. R. Astron. Soc.* **402**, 589 (2010).
- [68] M. Lo Verde, A. Miller, S. Shandera, and L. Verde, *J. Cosmol. Astropart. Phys.* **04** (2008) 014.
- [69] T. Y. Lam and R. K. Sheth, *Mon. Not. R. Astron. Soc.* **398**, 2143 (2009).
- [70] M. Maggiore and A. Riotto, *Mon. Not. R. Astron. Soc.* **405**, 1244 (2010).
- [71] S. Blinnikov and R. Moessner, *Astron. Astrophys.* **130**, 193 (1998).
- [72] N. Afshordi and A.J. Tolley, *Phys. Rev. D* **78**, 123507 (2008).
- [73] J.F. Navarro, C. S. Frenk, and S. D. M. White, *Astrophys. J.* **490**, 493 (1997).
- [74] J. S. Bullock, T. S. Kolatt, Y. Sigad, R. S. Somerville, A. V. Kravtsov, A. A. Klypin, J. R. Primack, and A. Dekel, *Mon. Not. R. Astron. Soc.* **321**, 559 (2001).
- [75] W.H. Press, S. A. Teukolsky, W. T. Vetterling, and B. P. Flannery, *Numerical Recipes in FORTRAN. The Art of Scientific Computing* (Cambridge University Press, Cambridge, England, 1992), 2nd ed.
- [76] R. W. Hockney and J. W. Eastwood, *Computer Simulation Using Particles* (Hilger, Bristol, 1988).
- [77] S. Johnson and M. Frigo, <http://www.fftw.org/> (2008).
- [78] N. Hamaus, U. Seljak, V. Desjacques, R. E. Smith, and T. Baldauf, *Phys. Rev. D* **82**, 043515 (2010).
- [79] P. Valageas and T. Nishimichi, [arXiv:1009.0597](https://arxiv.org/abs/1009.0597).